Chemical Engineering Journal 539 (2026) 176536

Contents lists available at ScienceDirect

Chemical Engineering Journal

journal homepage: www.elsevier.com/locate/cej

Comprehensive study of 3D liquid flow fields in additively manufactured structures for SMART reactors using large-scale vertical magnetic resonance imaging and computational fluid dynamics

Timo Merbach [a,*], Muhammad Adrian [b], Christoph Wigger [a], Selma Iraqi Houssaini [a], Benedict Bayer [a], Artyom Tsanda [c,d], Serhan Acikgöz [e], Christian Weiland [a], Felix Kexel [a], Dirk Herzog [e,f], Marko Hoffmann [a], Ingomar Kelbassa [e,f], Tobias Knopp [c,d,g], Alexander Penn [b], Michael Schlüter [a]

[a] Institute of Multiphase Flows, Hamburg University of Technology, Eißendorfer Straße 38, 21073 Hamburg, Germany
[b] Institute of Process Imaging, Hamburg University of Technology, Denickestraße 17, 21073 Hamburg, Germany
[c] Institute for Biomedical Imaging, Hamburg University of Technology, Am Schwarzenberg-Campus 3, 21073 Hamburg, Germany
[d] Section for Biomedical Imaging, University Medical Center Hamburg-Eppendorf, Lottestraße 55, 22529 Hamburg, Germany
[e] Institute for Industrialization of Smart Materials, Hamburg University of Technology, Harburger Schloßstraße 28, 21079 Hamburg, Germany
[f] Fraunhofer Research Institution for Additive Manufacturing Technologies IAPT, Am Schleusengraben 14, 21029 Hamburg, Germany
[g] Fraunhofer Research Institution for Individualized Medical Technology and Engineering IMTE, Mönkhofer Weg 239a, 23562 Lübeck, Germany

ARTICLE INFO

Dataset link:
https://doi.org/10.15480/882.16072

Keywords:
Porous media
Magnetic resonance imaging
Computational fluid dynamics
Triply periodic minimal surfaces

ABSTRACT

Triply Periodic Minimal Surface (TPMS) structures have emerged as a new class of porous materials with variable geometries and favourable transport properties, making them promising for reactor internals in chemical engineering. However, experimental data on internal TPMS flow behaviour are still limited. To address this gap, the flow behaviour in additively manufactured TPMS structures is analysed using three-dimensional Magnetic Resonance Imaging (MRI) velocimetry in a large-bore vertical 3 T MRI system, in cylindrical columns of 38 mm diameter and Reynolds numbers between 50 and 300. Three different TPMS geometries are investigated, and consistency between Computational Fluid Dynamics (CFD) simulations and experimentally measured MRI velocity fields is established through cross-validation. The MRI system provides fully three-dimensional velocity fields with a divergence deviation below 4 %. MRI revealed distinct flow features: the Gyroid TPnS exhibited pronounced channelling, while the Schwarz-Diamond TPSf showed merge-split behaviour, achieving a 46 % increase in lateral mixing compared to the Gyroid TPnS structures. Numerical simulations reproduce the flow features and show agreement with the MRI data. The combined methodology demonstrates the suitability of MRI velocimetry for the experimental validation of CFD simulations and establishes a robust foundation for future studies of heat and mass transfer, as well as reactive flow, in structured reactor systems.

1. Introduction

Structured internals are widely applied in chemical engineering to enhance reactor performance compared with packed beds [1–4]. Their implementation, particularly in chemical and biochemical reaction systems with catalytically active surfaces, improves heat and mass transfer, increases process efficiency through higher volume-specific surface areas, and enhances product selectivity [2,5,6].

While structured internals are designed to improve flow and transport properties, many industrially relevant chemical processes rely on fixed-bed reactors, which are characterised by randomly packed particles [7]. Such conventional reactors often face several operational limitations, including high pressure drops, dead zones, bypasses, uneven flow distribution, and consequently non-uniform access to the catalytic surface. Furthermore, the random packing of catalyst particles restricts scalability, while offering only limited flexibility in reactor design [1]. To address these limitations, structured reactor concepts such as monolithic reactors are already in use. These systems consist of arrays of parallel channels with catalytically coated walls, providing

* Corresponding author.
E-mail address: timo.merbach@tuhh.de (T. Merbach).

https://doi.org/10.1016/j.cej.2026.176536
Received 3 February 2026; Received in revised form 17 April 2026; Accepted 21 April 2026
Available online 24 April 2026

low pressure drops and well-defined flow paths [1]. However, the absence of cross-mixing between adjacent channels can limit their overall efficiency. Exchange between neighbouring channels can be achieved through so-called membrane catalysts, where transport predominantly occurs by diffusion, often resulting in mass-transfer limitations [1,6].

An emerging alternative to these conventional reactor designs is the implementation of geometries based on Triply Periodic Minimal Surfaces (TPMS), which overcome the limitations of both randomly packed beds and monolithic reactors [8]. These analytically defined periodic implicit surfaces are generated from combinations of trigonometric functions and contain no sharp edges or junctions. As a consequence, they exhibit zero mean curvature and form smooth geometries [5,9]. Moreover, these structures offer high design flexibility, as their volume-specific surface area, porosity, and the geometry itself can be adjusted flexibly [5]. TPMS-based architectures combine high mechanical stability with extensive interfacial area and favourable transport characteristics. Their interconnected channel networks promote homogeneous reactant distribution, enhanced mixing, and efficient heat and mass transfer [4–6,10]. Recent advances in additive manufacturing have transformed the production of complex geometries through a layer-by-layer material deposition process [11]. This enables the manufacturing of TPMS structures with high precision and reproducibility from diverse materials such as metals or polymers, making them particularly advantageous for applications in reaction and heat transfer engineering [12].

The Collaborative Research Centre 1615 *SMART Reactors*, funded by the German Research Foundation (DFG), aims to develop novel reactor concepts capable of addressing the challenges of future chemical engineering applications. These reactor systems are engineered for sustainable and autonomous operation, exhibiting high adaptability to fluctuating process conditions due to the varying quality of renewable reactants. Achieving such performance requires precise definition and control of the reactor geometry, since the internal structure fundamentally governs fluid dynamics, mixing behaviour, and mass transfer. Consequently, understanding the flow behaviour within the geometries of TPMS is essential for characterising flow patterns and local transport phenomena, which ultimately influence reaction yields. TPMS structures induce flow disturbances by geometry enhancing both heat and mass transport, making such structures particularly well-suited for applications in reactors [10]. To characterise these flow patterns, suitable non-invasive measurement techniques are required.

Established non-invasive flow measurement techniques such as Particle Image Velocimetry (PIV) and Particle Tracking Velocimetry (PTV) require optical access to the flow domain. Although PIV has been successfully applied to refractive index-matched porous media [13,14], and its application to TPMS structures has recently been demonstrated by Li et al. [15], these studies remain restricted to thin sections of the structures. This limitation arises from refractive index variations induced by the complex geometry, which lead to severe image distortion and limits visual accessibility.

Tomographic methods overcome the limitations of optical techniques, as they do not require optical access. For studies of TPMS structures, spatial resolution is a critical factor, since industrially relevant designs with high volume-specific surface areas feature fluid channel dimensions on the order of a few millimetres. Resolving the internal flow structures therefore requires sub-millimetre spatial resolution. In this context, several tomographic approaches have been employed for the study of liquid flows in porous media [16]. Electrical Capacitance Tomography (ECT) and its advanced form, Electrical Capacitance Volume Tomography (ECVT), are established techniques for flow imaging, with ECVT in particular having been applied to flow measurements in additively manufactured lattice structures [17]. However, both techniques do not provide sufficient spatial resolution to resolve the flow field within individual channels. Ultrasound tomography provides improved spatial resolution (2 mm) compared to ECT, and can in principle capture multiphase flow phenomena [16]. However, the strong scattering of acoustic waves at solid-liquid interfaces, as well as the internal geometry of TPMS, reduces signal quality and image reconstruction accuracy. Other tomographic approaches, such as gamma-ray and X-ray computed tomography, have been applied to flow imaging in columns with structured internals and periodic open-cell structures [16,18]. However, their spatial resolution is typically limited to the millimetre range, which is insufficient for resolving the flow field within TPMS structures [16,19]. In contrast, Magnetic Resonance Imaging (MRI) is an established method for flow measurements in chemical engineering [20,21]. MRI is based on the detection of the response of nuclear spins to magnetic fields and radiofrequency (RF) pulses [22]. Using phase-contrast velocity encoding techniques, MRI enables the quantification of three-dimensional velocity fields with sub-millimetre spatial resolution, making it suitable for studying fluid flow in TPMS structures [16]. Thus, numerous MRI studies have already been conducted to analyse the flow behaviour in porous media. For example, gas-liquid flows have been measured in packed beds and open-cell foams [23,24] and liquid flow through porous filters and particle fixed-beds have also been studied by MRI [25,26]. Also, MRI has been successfully applied to flow characterisation of TPMS structures, primarily focusing on the Schwarz-Diamond geometry [27–29]. By comparison, while the Gyroid is another widely studied TPMS geometry [10], its flow behaviour has not been investigated using MRI.

In the present study, the flow behaviour of three different additively manufactured TPMS geometries is characterised in a column with a diameter of 38 mm using a large-bore vertical 3 T MRI system, with three-dimensional velocity fields acquired with Reynolds numbers between 50 and 300. In porous media, the Reynolds number Re_S is defined using an appropriate characteristic length, most commonly the hydraulic diameter D_h [6]. Accordingly, it can be expressed as

$$Re_S = \frac{\rho w_S D_h}{\eta \epsilon}\,, \tag{1}$$

with ρ corresponding to the fluid density, η to the dynamic viscosity of the fluid, w_S to the superficial velocity, and ϵ to the porosity [30].

Unlike previous studies, the present work addresses both Schwarz-Diamond and Gyroid-based structures, thereby closing gaps in the literature and advancing the field. Furthermore, this study demonstrates the impact of unit cell geometry on the flow behaviour by rotating the unit cell in the Gyroid-based structure. Unit cell rotation is known to alter the mechanical properties of Gyroid structures [31]. Its influence on internal flow behaviour in TPMS structures has been investigated in previous numerical studies [32]. However, experimental studies of these effects, particularly using MRI, remains limited.

Beyond the investigated geometries, this work advances previous studies by enabling measurements in TPMS structures with a larger column diameter of 38 mm while maintaining a small hydraulic diameter, the relevant characteristic length for complex geometries. The use of a large-bore MRI system makes such measurements feasible. Small hydraulic diameters correspond to a high volume-specific surface area, making them particularly relevant for chemical engineering applications. In previous MRI-based studies, measurements have been conducted in TPMS structures with hydraulic diameters of 2 mm and 7.2 mm and corresponding column diameters of 9 mm and 29.5 mm, resulting in ratios of column diameter to hydraulic diameter ranging from 4.1 to 4.5 [27–29]. In contrast, the present configuration achieves a ratio of up to 10.4, thereby extending the accessible scale for MRI-based flow characterisation in TPMS structures. Thus, this setup not only represents a 30 % larger geometry than previously reported in MRI studies on TPMS, but also contains a larger number of inner channels. In addition to experimental MRI velocimetry, Computational Fluid Dynamics (CFD) is also subject of research for studying flow behaviour through TPMS structures. However, CFD simulations require validation to ensure that the predicted flow fields represent real systems. Traditionally, these simulations are validated using integral quantities such as pressure drop, since direct measurements of three-dimensional velocity fields in complex porous geometries are difficult to obtain [33–35].

MRI allows macroscopic flow characterisation by experimentally measuring spatially resolved velocity fields. Previous studies have shown that combining CFD simulations with experimental MRI measurements is beneficial, as the experimental data can be directly compared with CFD results [36–38]. In this study, the combination of both methods enables cross-validation, whereby the CFD simulations are validated using MRI measurements and vice versa.

The structure of the paper is as follows: Section 2 introduces the studied TPMS structures, experimental and computational setups used in the present work. Sections 3.1 and 3.2 are dedicated to the validation of the MRI system through quantitative assessments, including structural integrity, mass flow rate and the divergence-free criterion. Additionally, Section 3.3 presents an analysis that combines the qualitative identification of characteristic flow structures with vorticity as a quantitative flow metric. Finally, consistency between the CFD simulations and the MRI measurements is established through cross-validation in Section 3.4.

2. Methods

The selection and fabrication of the used TPMS is addressed in the following. Both, the experimental and the computational setups are presented. Further, the methods and principles concerning the fluid dynamics and the MRI-based flow measurements are investigated.

2.1. Selection and manufacturing of TPMS

In this study, three distinct TPMS structures are examined as porous internals for chemical engineering applications. TPMS are mathematically defined as infinitesimally thin surfaces. For the manufacturing, these geometries must be adapted either by assigning a finite wall thickness to the surface or by considering the volumes enclosed by the surfaces as the solid domain. Following the nomenclature of Fisher et al. [39], TPMS structures can be classified into skeletal structures, including Triply Periodic endo-Skeleton (TPnS) and Triply Periodic exo-Skeleton (TPxS), where the volume defined by the surface is considered as the solid domain. In addition, surface-type structures, referred to as Triply Periodic Surfaces (TPSf), are defined, where the surface with a finite thickness represents the solid part of the unit cell. Two unit cells, a Gyroid TPnS and a Schwarz-Diamond TPSf, are generated. In addition to the standard Gyroid TPnS, a Gyroid TPnS geometry rotated by 45° (see Fig. 1 for the definition of the angle orientation) is also examined, as this configuration is expected to exhibit improved flow characteristics, as discussed in the following. All unit cells are illustrated in Fig. 1.

After selecting the type of unit cell, each TPMS is characterised by three key parameters: the sheet thickness, the porosity, and the unit cell size, defined as the edge length of a three-dimensional cube. In this paper, all structures exhibit a unit cell size of $10 \times 10 \times 10$ mm^3 and a porosity of $\epsilon = 70$ %, which can be chosen independently of one another. Consequently, the sheet thickness follows as the dependent variable of the other two.

The two types of TPMS structures studied in this work differ primarily in their number of nodes and channels, as well as in their volume-specific surface areas. Both structures exhibit high volume-specific surface areas a, with $a_G = 320$ m^2 m^{-3}, $a_{G45} = 322$ m^2 m^{-3} and $a_{SD} = 767$ m^2 m^{-3}, making them particularly suitable for heterogeneous catalysis and heat-transfer applications. The larger volume-specific surface area of the Schwarz-Diamond TPSf structure primarily arises from the different TPMS representation. While the Schwarz-Diamond TPSf is modelled as a surface-type TPMS, the Gyroid TPnS is implemented as an endo-skeleton structure. Consequently, at identical porosity, the Schwarz-Diamond TPSf structure exhibits an increased specific surface area. This effect is also reflected in the hydraulic diameter, which is defined as

$$D_h = 4\epsilon \frac{V_W}{A_{W,S}} = \frac{4\epsilon}{a}, \quad (2)$$

where V_W denotes the wetted (free) volume and $A_{W,S}$ the wetted surface area [30]. For the selected structures, the corresponding geometric properties are determined using nTopology (*nTopology Inc., USA*), yielding in hydraulic diameters of $D_{h,G} = 8.8$ mm for the Gyroid TPnS, $D_{h,G45} = 8.7$ mm for the rotated Gyroid TPnS, and $D_{h,SD} = 3.7$ mm for the Schwarz-Diamond TPSf structure. Notably, the hydraulic diameter of the Schwarz-Diamond TPSf is approximately 43 % of that of the Gyroid TPnS. Accordingly, the observed differences in specific surface area between the structures essentially result from their differing hydraulic diameters and the chosen TPMS representations (TPnS versus TPSf), rather than from the specific topology (Gyroid versus Schwarz-Diamond) itself.

The Schwarz-Diamond geometry has already been employed in studies of heterogeneous catalysis [40]. Previous studies have also shown that the Gyroid-based structure outperforms conventional monolithic designs in terms of yield and mass-transfer performance, resulting in higher overall efficiency [8]. Moreover, the Gyroid geometry achieves superior heat-transfer rates under turbulent flow conditions, whereas the Schwarz-Diamond exhibits excellent thermal performance even under laminar conditions [41]. These favourable properties arise not only from the high volume-specific surface areas but also from the tortuous geometry of the structures. Both Schwarz-Diamond and Gyroid structures exhibit intensified mixing and flow homogenisation [10]. The geometric configuration of the Gyroid structure generates helical flow patterns in both clockwise and counter-clockwise directions, while the Schwarz-Diamond TPSf additionally produces characteristic merge-split flow patterns [10]. Although both structures exhibit pressure drops of similar magnitude at low Reynolds numbers [10,42], the Gyroid TPnS inherently induces channelling effects due to its continuous pathways aligned with the main flow direction [43]. To counteract this tendency and enhance lateral mixing, a Gyroid TPnS rotated by $\alpha = 45°$ around the y-axis is therefore included in the analysis (see Fig. 1(b)). As stated in Section 1, the impact of unit cell rotation on internal flow behaviour has been studied numerically for TPMS structures [32] and is addressed in the present study experimentally. To investigate such geometric effects, the TPMS structures considered in this work are constructed by periodic replication of a single unit cell, as described below.

Starting from the individual unit cell, the complete structures for the study are generated. Fig. 2 illustrates the generation process shown here using Gyroid TPnS ($\alpha = 0°$) as an example. The structures are designed using nTopology, beginning with the individual unit cell design (see Fig. 2(a)). Subsequently, rectangular blocks are generated and cut into cylindrical geometries with an inner diameter of $D = 38$ mm (DN 40 in accordance with DIN 11866 [44]) and a length of $L_M = 100$ mm (see Fig. 2(b)). These cylindrical structures are then integrated with a surrounding wall and clamping connectors in accordance with DIN 32676 [45] (see Fig. 2(c)). In addition, the Field Of View (FOV) for the MRI measurements is illustrated, with further details provided in Sections 2.2 and 2.3. After the design process, the entire structure is fabricated in a single step to eliminate the channelling effects between the structure and the surrounding wall. Moreover, this approach represents real reactor configurations, as the integrated wall enhances heat transfer under both heating and cooling conditions [4,11].

The Gyroid TPnS ($\alpha = 0°$) structure is fabricated by Laser-Based Powder Bed Fusion of Polymers (PBF-LB/P) as defined in DIN EN ISO/ASTM 52900:2022-03 [46], often also referred to as Selective Laser Sintering (SLS), using an EOS Eosint P396 system (*EOS GmbH, Germany*). In this process, a laser selectively melts layers of polyamide 12 powder (median particle diameter of $d_{50} = 51 - 61$ µm) to form the final structure. After fabrication, the part is cleaned by sandblasting to remove residual powder.

However, a limitation of this technique is the removal of unsintered powder from geometries without continuous channels and limited accessibility due to the surrounding wall. As a result, complete powder removal could not be achieved for the Schwarz-Diamond TPSf

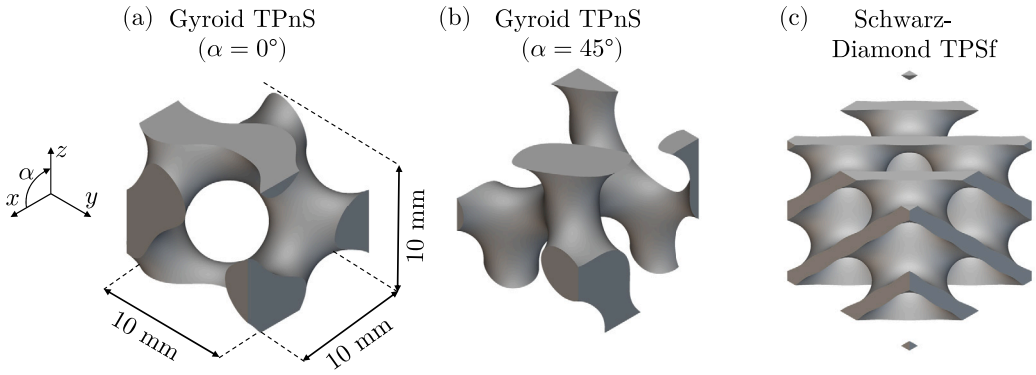

Fig. 1. Unit cells employed in this study: (a) Gyroid TPnS ($\alpha = 0°$) (G), (b) Gyroid TPnS ($\alpha = 45°$) (G45), and (c) Schwarz-Diamond TPSf (SD). All structures exhibit a porosity of $\epsilon = 70$ % and a unit cell size of $10 \times 10 \times 10$ mm^3.

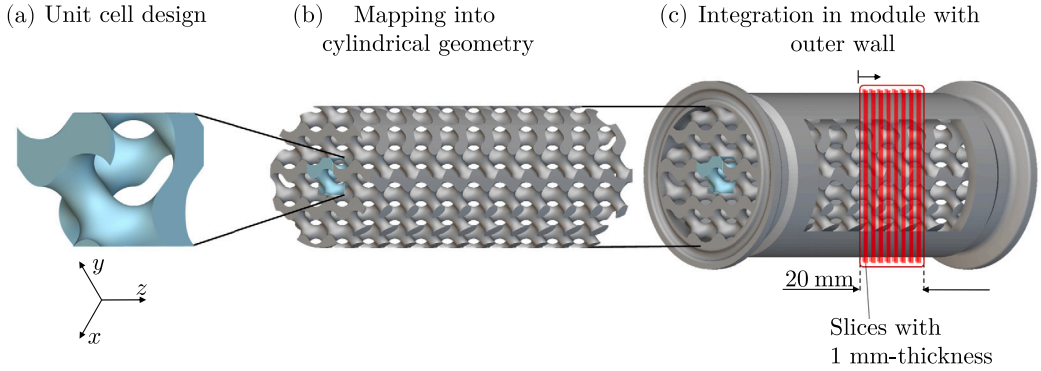

Fig. 2. Generation process of the structures, exemplified by the Gyroid TPnS ($\alpha = 0°$). (a) Unit cell design. (b) Assembly of the structure as a rectangular block and subsequent mapping into a cylindrical geometry. (c) Integration of the surrounding wall and clamping connectors into the cylindrical design. The red section indicates the FOV for the MRI measurements, covering a length of 20 mm with 20 slices of 1 mm thickness. For clarity, the figure shows a reduced number of slices.

and rotated Gyroid TPnS structures following the PBF-LB/P process. Therefore, these two structures are fabricated using a Formlabs Form 3+ system (*Formlabs, USA*), which employs Vat Photopolymerisation, curing by Ultra Violet Laser beam exposure (VPP-UVL) according to ISO standard [46]. In this process, often also referred to as stereolithography (SLA), a photosensitive polymer (Clear V4 resin (*Formlabs, USA*)) is cured layer by layer to build the TPMS modules. The VPP-UVL printer provides a spatial resolution of 0.25 mm, and the prints are fabricated without internal support structures.

The main distinction between the two manufacturing methods lies in the surface quality. Since PBF-LB/P relies on a powder-based process, the resulting surface is rougher compared to the smooth surface obtained via VPP-UVL. However, the influence of surface roughness on the macroscopic flow behaviour is expected to be negligible. The roughness, which is expected to correspond approximately to the median particle diameter of the powder, remains well below the selected spatial resolution of the MRI (see Section 2.3) and therefore does not introduce measurement bias on the scale relevant to this study. Consequently, both materials remain fully suitable for MRI-based flow analysis, and the comparison with CFD is not affected.

2.2. Experimental setup and fluid system

The experimental setup to investigate the flow behaviour within the TPMS structures is shown in Fig. 3. It consists of a gear pump (1) (*Gather Industries GmbH, Germany*), a Coriolis Mass Flow Meter (MFM, 2) (*Endress & Hauser, Germany*) for monitoring the mass flow rate. According to the manufacturer, the measurement deviation of the MFM is less than ±1.25 % of the measured mass flow rate [47]. A degassing vessel (3) (*Binder GmbH, Germany*) is connected to a vacuum pump (4) (*Edwards Vacuum, UK*), and an acrylic pipe (5) is installed, followed by the TPMS modules (6) analysed in this study, as introduced in Section 2.1. The upstream acrylic pipe has an inner diameter of $D = 38$ mm (DN 40) and a length of $L_E = 760$ mm. This length helps to minimise the influence of upstream flow development and capture intrinsic flow characteristics within the TPMS structures. Two TPMS modules, each $L_M = 100$ mm in length, are mounted downstream of the acrylic pipe and connected using nylon BioClamps (*BioPure Technology Ltd, UK*) as clamping connections.

The acrylic pipe together with the mounted structures is positioned inside the MRI system (7) for analysis. Moreover, Fig. 3 provides a close-up view of the experimental setup with the RF receive coil (8), which has a clip-on feature for easy switching between different structures. The FOV (9) for the MRI measurements is highlighted in accordance with Fig. 2. Measurements are taken in the centre of the second module, approximately after a length of $L_{E,M} = 150$ mm downstream, where sufficient momentum exchange with the structure ensures that the flow conditions are independent of the inlet effects. This observation is consistent with the findings of Hawken et al. indicating that entrance effects are negligible for $L_{E,M} > 11 D_h$, where D_h denotes the hydraulic diameter defined in Eq. (2) [48].

The working fluid is deionised water supplemented with copper sulphate pentahydrate (*Carl Roth GmbH + Co. KG, Germany*, CAS: 7759-99-8, purity ≥ 98 %) at a concentration of $c_{CuSO_4} = 34$ mmol L^{-1}, which has beneficial effects for MRI measurements, as discussed in Section 2.3. The used fluid is maintained at a temperature of $T = (25 \pm 1)$ °C with a density of $\rho = (1002.9 \pm 0.3)$ kg m^{-3}, interpolated from [49,50], and a viscosity of $\eta = (0.890 \pm 0.020)$ mPa s [50]. For the

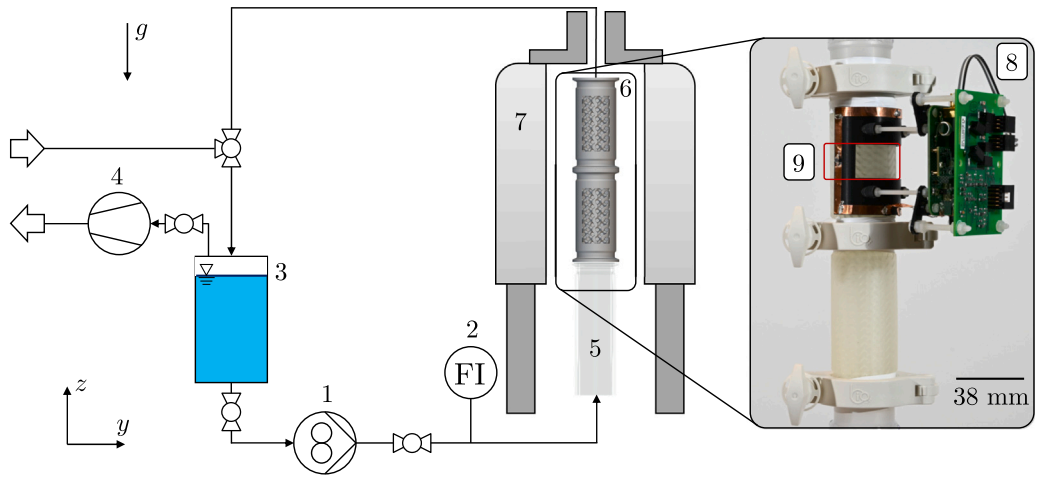

Fig. 3. Left: Schematic flow diagram of the experimental setup showing the gear pump (1), the Coriolis MFM (2) for monitoring the mass flow rate, the degassing vessel (3) with the vacuum pump (4), the inlet acrylic pipe (5), the TPMS modules (6), and the MRI system (7). The main flow direction through the TPMS modules is oriented opposite to the gravitational acceleration g. Right: Close-up of the analysed area is illustrated, including the custom-built RF receive coil with single-channel (8) and the FOV within the module (9).

Table 1
Operating conditions, including mass flow rate $\dot{M}$, superficial velocity w_S, and Reynolds number for porous media Re_S for the three operating points.

Mass flow rate $\dot{M}$ / kg min^{-1}	0.755 ± 0.03	1.15 ± 0.01	1.50 ± 0.01
Superficial velocity w_S / mm s^{-1}	11.1	16.9	22.0
Reynolds number for porous media Re_S / –			
Gyroid TPnS($\alpha = 0°$) (G)	156	237	310
Gyroid TPnS($\alpha = 45°$) (G45)	155	236	308
Schwarz-Diamond TPSf (SD)	65.0	99.1	129

viscosity, the value of pure water is used, as a minor addition of copper sulphate is estimated to cause a deviation of less than 2 % [50,51]. The standard deviation is indicated by ± throughout this paper.

The working fluid is pumped from the degassing vessel through the gear pump and then through the TPMS modules. Before each experiment, it is essential to ensure that no gas bubbles remain within the structures, as they may distort the flow field by blocking channels or adhering to internal surfaces. The narrow channels and tortuous pathways of the TPMS geometries promote bubble accumulation, and therefore a dedicated procedure is applied to minimise bubble entrapment. For each experiment, the degassing vessel is filled with the working fluid, sealed, and evacuated using the vacuum pump until an absolute pressure of $p < 20$ mbar is reached and maintained for at least 20 minutes. This step removes dissolved gases that would otherwise emerge within the structures due to pressure drops during operation. The vessel is subsequently returned to atmospheric pressure ($p = 1.013$ bar), and the valves are adjusted to establish a closed-loop circulation of the working fluid. The remaining bubbles are eliminated by repeated cycles of oscillatory volume fluxes. The degassing procedure is repeated until no bubbles are visible in the MRI images and no gas release is observed after the modules. Once a bubble free state is reached, MRI measurements are initiated.

Measurements are performed under different operating conditions that are characterised by varying superficial velocities. Table 1 summarises the operating conditions, including the measured mass flow rate $\dot{M}$, the superficial velocity w_S in the empty pipe, and the Reynolds number within the structures Re_S (see Eq. (1)). For all operating conditions studied in the Schwarz-Diamond TPSf geometry (see Table 1), the Reynolds number ranges from $10 \lesssim Re_S \lesssim 150$, corresponding to the Darcy-Forchheimer regime, in which (non-linear) laminar flow prevails [24,52]. In contrast, the Reynolds numbers for the Gyroid TPnS structures fall within $150 \lesssim Re_S \lesssim 300$, corresponding to the post-Forchheimer regime in which unsteady flows with laminar wake oscillations occur. Above $Re_S \approx 250$, vortex formation occurs, and for $Re_S \gtrsim 300$, the flow transitions to a turbulent regime, with the flow patterns start with characteristics typical to classical turbulent flow [52,53]. The structures are primarily analysed and compared within the Darcy-Forchheimer regime, where the flow remains laminar.

2.3. MRI velocimetry

MRI velocimetry measurements are performed on a worldwide unique large-bore 3 T vertical MRI system with an inner diameter of 400 mm located at Hamburg University of Technology. The vertical configuration of the MRI offers several experimental advantages: it allows the study of longer setups with larger diameters, while maintaining a flow orientation consistent with most process equipment such as plug flow reactors or distillation columns. Moreover, gas bubbles can rise naturally, preventing their accumulation in the measurement section and avoiding artefacts in the recorded velocity fields.

The MRI system is equipped with a birdcage RF coil for homogeneous signal excitation and a custom-built single-channel RF receive coil for signal detection. Measurements are conducted in the FOV inside of the structures, which is illustrated in Figs. 2(c) and 3. The setup is placed so that the FOV is positioned at the isocentre of the scanner to ensure maximal magnetic field homogeneity. A copper sulphate solution (see Section 2.2) is used as the working fluid due to its relaxation properties for MRI-based flow measurements [54]. At the used copper sulphate concentration, the solution yields a short longitudinal (spin-lattice) relaxation time of $T_1 = 20$ ms [55,56], measured using a 60 MHz benchtop Nuclear Magnetic Resonance (NMR) spectrometer (*Spinsolve 60, Magritek, Germany*). The short relaxation time T_1 enables fast re-excitation of the spin system, which is essential for time-efficient MRI velocimetry [57]. It should be noted that the NMR measurements are performed at approximately 1.5 T (60 MHz corresponds to 1.4 T), whereas the MRI experiments are conducted at 3 T, which affects the T_1 value. However, for liquid systems, this difference is generally small and unlikely to significantly influence T_1. This is consistent with NMR relaxation theory, which predicts only weak field dependence of T_1 in mobile aqueous systems [58–60].

MRI-derived velocity fields are quantified by using bipolar flow-encoding gradients, which encode coherent spin motion as velocity-dependent phase shifts in the MR signal [27]. The resulting phase is directly proportional to the local fluid velocity and is used to compute spatially-resolved velocity fields [61]. Background phase corrections

Table 2
Overview of MRI acquisition parameters and Velocity Encoding (VENC) settings for used TPMS geometries at operating conditions.

Parameter	Value
Scan mode	Multi-2D
Slice orientation	Transverse
Phase-encoding direction	y
Flip angle / ∘	90
Water-fat shift / pixel	0.91
Number of scan averages	1
FOV (x, y, z) / mm	40, 40, 20
Voxel size (x, y, z) / mm	0.25, 0.25, 1
Velocity Encoding (VENC) $x - y - z$ / mm s^{-1}	
Gyroid TPnS ($\alpha = 0°$)	
$Re = 156$	40 – 40 – 80
$Re = 237$	60 – 60 – 120
$Re = 310$	110 – 110 – 200
Gyroid TPnS ($\alpha = 45°$)	
$Re = 155$	80 – 80 – 160
$Re = 236$	120 – 120 – 210
$Re = 308$	110 – 110 – 200
Schwarz-Diamond TPSf	
$Re = 65.0$	140 – 60 – 90
$Re = 99.1$	150 – 80 – 100
$Re = 129$	200 – 100 – 150

are neglected, as initial investigations indicated no measurable impact on the results. Measurements are conducted using a gradient echo pulse sequence with a Multi-two-Dimensional (M2D) acquisition method, enabling three-dimensional reconstruction of the velocity fields within the TPMS structures. The pulse sequence used for data acquisition is the *Quantitative Flow* (*QFlow*) sequence provided by Philips (*Philips N.V., Netherlands*), based on spoiled gradient-echo sequence. An overview of the acquisition parameters used for the flow protocol is provided in Table 2. These parameters are carefully selected to ensure a high Signal-to-Noise Ratio (SNR) within the allowable range of each parameter [62,63]. Flow-compensation is not employed, as preliminary evaluations indicated no measurable impact on the results. Further measurement parameters employ a flip angle of 90°, an echo time ranging from 5.4 ms and 6.8 ms depending on the Velocity Encoding (VENC), and a repetition time of 150 ms.

The measurements are obtained with a spatial resolution of 0.25×0.25 mm^2 in the lateral plane, corresponding to a pixel-to-millimetre ratio of 4.4 px mm^{-1}. The FOV in the lateral plane is 40×40 mm^2, while the slice thickness is 1 mm per slice. Consecutive slices are recorded along the axial direction, covering a total distance equivalent to twice the unit cell length (20 mm) (see Fig. 2(c)). The total acquisition time for the measurement per operating flow rate condition is approximately 32 min. In this study, a high spatial resolution of 250 µm in lateral direction is chosen to resolve the channels inside the TPMS structures. The achievable temporal resolution restricts the analysis to time-averaged flow quantities, and the flow is therefore considered to be in a statistically steady state.

The Velocity Encoding (VENC) gradient strength is adjusted in line with the prevailing flow conditions, and the associated pulse sequence parameters are modified accordingly. The VENC values corresponding to the different operating conditions are summarised in Table 2. While increasing flow velocity enhances phase contrast, the overall SNR in the magnitude image decreases with higher flow rates due to flow-related dephasing and reduced signal coherence within a voxel. Consequently, despite the increased phase contrast, the reduced magnitude SNR limits the precision of the velocity estimation [63–65].

An additional aspect concerns material-related effects. The TPMS modules are fabricated from two different materials. Magnetic susceptibility differences between the two material types, as reported by Sangal et al. [66], may become apparent in gradient-echo sequences. However, susceptibility matching is not targeted, as the focus of this study is on improving signal quality, but will be addressed in future works. The selected liquid medium is chosen to reduce T_1, thereby increasing SNR, improving the Velocity-to-Noise Ratio (VNR), and enabling shorter acquisition times [63].

2.4. Fluid-dynamic fundamentals

MRI-based flow measurement is a well-established technique. However, validation is essential in MRI velocimetry because measurement uncertainty and biases can arise from imposed assumptions, signal noise, and imperfections in the experimental setup. To ensure the reliability of the results, the validation of the measured velocity fields is performed using fundamental fluid-dynamic principles. From the three-dimensional velocity field, the mass flow rate $\dot{M}$ can be determined and directly compared with the measured value from the MFM. The mass flow rate is obtained from the data by multiplying the fluid density by the axial velocity $w(x, y)$ integrated over the free cross-sectional area A_S [27,67]. In the case of discrete data, the axial velocity of each pixel $w_i(x, y)$ is multiplied by the area of pixel $A_P = 0.0517$ mm^2 px^{-1} and the fluid density. The sum of all pixels n yields in

$$\dot{M} = \rho \iint_{A_S} w(x, y) \mathrm{d}A \approx \rho \sum_{i=1}^{n} \left(w_i(x, y) \right) A_P. \tag{3}$$

Since the mass flow rate validates only for the axial component of the velocity, while MRI velocimetry and CFD provide all three velocity components, the divergence is additionally assessed. For incompressible fluids, the velocity field must satisfy the divergence-free condition for the velocity field $\boldsymbol{u}$

$$\mathrm{div}\, \boldsymbol{u} = \frac{\partial u}{\partial x} + \frac{\partial v}{\partial y} + \frac{\partial w}{\partial z} = 0\,, \tag{4}$$

where u, v, and w represent the velocity components in the x-, y-, and z-directions, respectively [67]. Both Eqs. (3) and (4) are used to assess the physical consistency of the MRI-derived velocity data and thus serve as validation criteria.

Furthermore, the vorticity ω_z, defined as

$$\omega_z = \frac{\partial v}{\partial x} - \frac{\partial u}{\partial y}\,, \tag{5}$$

is evaluated [67]. It serves as a key measure of rotational flow structures. Due to the discrete nature of the data, spatial derivatives are evaluated using finite-difference schemes, with second-order central differences applied in the interior and first-order one-sided differences at the boundaries. These operations are implemented in MATLAB (*MathWorks Inc., USA*) using the built-in `gradient` function to estimate the spatial gradients. In addition to the local flow analysis based on differential operators, the hydraulic tortuosity T_h is introduced as a macroscopic quantity. It is defined as

$$T_h(z) = \frac{\sum_{i=1}^{n} |\boldsymbol{u}_i(x, y, z)|}{\sum_{i=1}^{n} w_i(x, y, z)}\,, \tag{6}$$

where $|\boldsymbol{u}_i(x, y, z)|$ is the magnitude of the velocity vector and $w_i(x, y, z)$ is the axial velocity at the lateral position of each in-plane position x, y [68]. n denotes the number of pixels, and z corresponds to the slice location. The hydraulic tortuosity serves as a measure of the deviation of the flow from the axial direction and, consequently, characterises the degree of lateral mixing within the structure [27,68].

2.5. Computational setup

The numerical flow simulations are conducted using the same Computer-Aided Design (CAD) models that served as the basis for additive manufacturing. Thus, the computational domain comprises two cylindrical elements shown in Fig. 2(c), supplemented by an additional pipe section to ensure the development of an established

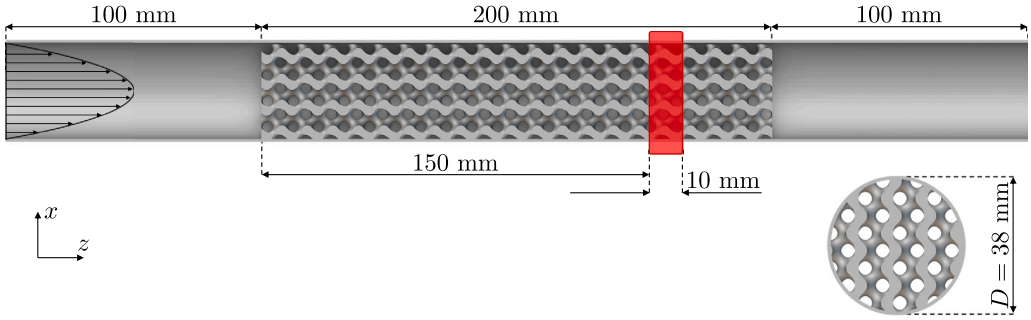

Fig. 4. Full-scale CFD configuration with an established flow profile, highlighting the analysed FOV (red), shown for the Gyroid TPnS ($\alpha = 0°$) structure.

flow profile, together with an outlet section (see Fig. 4). Moreover, the simulations are performed under the same operating conditions as the experiments.

All numerical simulations are performed using the open-source software *OpenFOAM* (Version 2406) with the *simpleFoam* solver, steady state flow conditions as indicated by the MRI measurement. Inlet velocity and pressure outlet boundary conditions are applied in addition to standard wall boundary conditions at the acrylic pipe and the TPMS modules, including a no-slip condition. The flow field is initialised with a parabolic velocity profile corresponding to the respective operating point. The initial pressure field is set to a uniform 0 Pa gauge pressure, as for incompressible media, the pressure levels are relative to a reference pressure. During initialisation first-order Gauss upwind schemes are employed for gradient and divergence terms, whereas for an accurate solution spatial discretisation is performed using the least squares method for gradients, Gauss QUICK schemes for divergence terms, and a second-order linear corrected scheme for Laplacian terms. Comprehensive information concerning the initial conditions, boundary conditions, numerical discretisation schemes, and solver settings are available in the associated research data [69].

Unstructured hexahedral meshes are generated using *snappyHexMesh*. Four progressively refined grids are prepared to assess the reliability of the simulation results with varying grid resolution

$$R^* = \frac{D}{\max(\Delta x, \Delta y, \Delta z)}\,, \tag{7}$$

where $D = 38$ mm corresponds to the characteristic length of the acrylic pipe (inner diameter) and Δx, Δy and Δz are the distance between nodes of the equidistant hexahedral mesh. It should be noted that R^* refers to the background mesh only and further local refinements are applied using *snappyHexMesh*. The convergence study has been conducted for the Gyroid TPnS ($\alpha = 0°$) with grid resolution $R^* \in \{20, 30, 40, 50\}$ [69]. To determine which grid resolution is sufficiently fine enough to deliver reliable and grid independent results, it is verified by the Grid Convergence Index (GCI) proposed by Roache [70]. The GCI serves as an indicator for assessing the optimal computational grid by estimating the discretisation error based on Richardson's extrapolation [71]. Since the pressure inherently depends on the overall momentum balance and energy dissipation of the flow, it is highly sensitive to the accuracy of the resolved velocity fields that characterise the fluid dynamic state, thereby making it a suitable parameter for assessing the GCI. The refinement factor r is computed for a set of simulation, consisting of a coarse, medium, and fine grid. The order of discretisation is determined iteratively for a set of grids to account for potential non-monotone convergence. For a set of three simulations, a fine GCI

$$\mathrm{GCI}^{12}_{\mathrm{fine}} = F_{\mathrm{S}} \cdot \frac{\varepsilon_{12}}{1 - r^P}\,, \tag{8}$$

and a coarse GCI

$$\mathrm{GCI}^{23}_{\mathrm{coarse}} = F_{\mathrm{S}} \cdot \frac{\varepsilon_{23}}{1 - r^P} \tag{9}$$

can be approximated by the Richardson error estimator with the convergence index P, the change of the numerical solution $\varepsilon_{ij} = f_i - f_j$ between two consecutively refined grids f_i and f_j, and a safety factor $F_{\mathrm{S}} = 1.25$. For grid studies considering three or more grid solution, this safety is adequately sufficient [70]. As shown in Table 3, the mesh configuration $R^* = 50$ exhibits an exceptionally low grid convergence index $\mathrm{GCI}^{23}_{\mathrm{fine}} = 2.721 \cdot 10^{-6}$, indicating that further grid refinement is not necessary. Therefore, a grid configuration ($R^* = 50$) is used for this study.

Table 3
Grid convergence index analysis for different mesh types, showing average mesh size, resulting pressure drop, and $\mathrm{GCI}_{\mathrm{fine}}$.

Grid resolution R^* / –	Average mesh size h / μm	Pressure drop Δp / Pa	$\mathrm{GCI}^{12}_{\mathrm{course}}$	$\mathrm{GCI}^{23}_{\mathrm{fine}}$
20	279.1	5.722	$3.520 \cdot 10^{-1}$	–
30	214.8	5.791	$1.351 \cdot 10^{-4}$	–
40	178.4	5.809	–	$1.630 \cdot 10^{-1}$
50	154.0	5.810	–	$2.721 \cdot 10^{-6}$

The numerical data are used for cross-validation with the MRI measurements. The simulations consist of spatially scattered data points containing velocity components at specified coordinates. MATLAB's built-in `scatteredInterpolant` function is applied to each velocity component in order to reconstruct a continuous velocity field. The velocity field is then interpolated onto a structured Cartesian grid with a defined spatial resolution. This resolution can be adapted to match the spatial resolution of the MRI data using MATLAB's `interp2` function, which performs linear interpolation to estimate values of a two-dimensional function at evaluation points. The resulting CFD velocity fields are generated of infinitesimal small slices generated at a spacing of 200 μm.

After obtaining a continuous velocity field for numerical data, the MRI data are aligned with the CAD geometry. Both the axial position within the TPMS structure and the orientation of the measured slice are determined for the experimental data. The MRI data are rotated and shifted laterally to match the orientation of the CFD dataset. MRI data have an axial spatial resolution of 1 mm (see Section 2.3), whereas the CFD velocity fields are defined on discrete planes. Thus, to allow direct comparison, the CFD data must be volumetrically averaged over the corresponding 1 mm slice thickness. Without this averaging, the geometric variations of the structure along the axial direction are not properly represented. To align the CFD and MRI datasets, a matching procedure is applied in which the mean deviation between the first MRI slice and the corresponding CFD slice is evaluated. The axial position of the CFD data is adjusted iteratively until the smallest mean deviation with the corresponding MRI slice is achieved. The subsequent slice pairs are assigned at 1 mm intervals along the axial direction. Starting from this position, 1 mm-thick CFD slices are subsequently extracted for cross-validation analysis.

3. Results and discussion

The validation of the MRI measurement system is carried out through quantitative checks of structural integrity, mass flow rate,

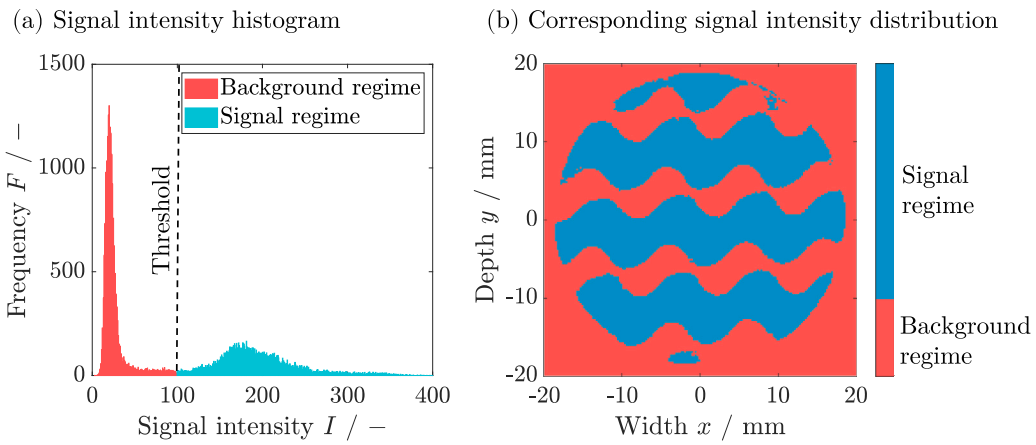

Fig. 5. The signal intensity is plotted as a histogram, exemplarily shown for the Gyroid TPnS ($\alpha = 0°$) at $Re_S = 156$ and $z = 0$ mm in (a) (see Table 1). The histogram of the signal intensity for a single slice shows two main peaks, with the local minimum used as a threshold to filter and retain only the flow signal. (b) shows the corresponding signal intensity distribution locally across the cross-sectional area.

and divergence-free condition. Building on this validation, the flow behaviour within the three TPMS structures is analysed, with emphasis on characteristic flow patterns and vorticity. MRI measurements are used to validate the CFD simulations and to assess the consistency between the experimental and numerical results.

3.1. Validation of structural integrity

The experimental MRI data are initially used to validate the additive manufacturing process by assessing the structural integrity of the printed modules using the signal intensity of the images. Visual inspection of the printed structures using the signal intensity of the images revealed no defects or anomalies in any of the modules. In addition to this qualitative assessment, a quantitative evaluation is performed by determining the cross-sectional area of each structure using MATLAB. This process consists of three steps: filtering of the data, binarisation of the signal intensity images, and comparison of the resulting cross-sectional area of the structures with the corresponding area obtained from the CAD files.

The data are first limited to the flow-relevant region of the domain according to the procedure described by Bruschewski et al. [72,73]. In this approach, the signal intensity is plotted against its frequency for each slice, as illustrated exemplarily in Fig. 5(a) for the Gyroid TPnS ($\alpha = 0°$) at $Re_S = 156$ (see Table 1) and $z = 0$ mm. In the complete analysis, the coordinate z denotes the axial position along the sample (length), where $z = 0$ mm corresponds to the first slice of the MRI acquisition. The lateral directions x and y denote width and depth, respectively.

Fig. 5(a) displays two prominent peaks: the lower-intensity peak corresponds to the background, encompassing the structure itself, motion artefacts, and artefact-free regions, whereas the higher-intensity peak represents the desired flow signal. The region between these peaks reflects partial volumes, i.e., voxels containing both fluid and solid material. Importantly, the partial volume region remains clearly distinguishable from the primary peaks. Given that both main peaks are larger than the partial volume contribution, it can be concluded that the spatial resolution is sufficiently high to enable an analysis of the structures [73]. Following the recommendation of Bruschewski et al. [72], the local minimum for each slice between the two dominant peaks is determined and applied as a threshold. The procedure can be confirmed using Fig. 5(b), which shows the corresponding cross-sectional area of the signal intensity distribution. Qualitatively, the regions corresponding to the signal regime, i.e. the flow regions, can be distinguished from the background regime.

As a reference, the arithmetic mean threshold values over the full axial range for the Gyroid TPnS ($\alpha = 0°$), Gyroid TPnS ($\alpha = 45°$), and Schwarz-Diamond TPSf structures are 0.26 ± 0.02, 0.20 ± 0.02, and 0.13 ± 0.01, respectively. For better comparability, the values have been normalised to the maximum value. Each two-dimensional slice is binarised using the threshold determined for that slice. The processed MRI data are compared with the CAD data to evaluate the correspondence of the cross-sectional areas. The cross-sectional area is derived from the CAD data, which serve as the basis for both additive manufacturing and CFD simulations. For a quantitative assessment, the cross-sectional areas are determined from both the MRI data and the CAD models. The results along the axial direction for two unit cell lengths, 20 mm, are presented in Fig. 6.

From the analysis of Fig. 6, the Gyroid TPnS structures with $\alpha = 0°$ and $\alpha = 45°$ show mean deviations of 16 % and 2.0 % between the CAD-derived and MRI-derived data, respectively. The Schwarz-Diamond TPSf exhibits a deviation of 15 % between the CAD-derived geometry and the MRI measurements, indicating that the datasets lie within the same order of magnitude and show overall agreement. The Gyroid TPnS ($\alpha = 0°$) maintains an almost constant cross-sectional area along its length with variations smaller than 4 %, which is reproduced by the MRI data. In contrast, the $\alpha = 45°$ configuration shows a pronounced axial variation in the cross-sectional area, well captured by MRI. For the Schwarz-Diamond TPSf geometry, the general signal intensity images agree with the CAD model, but the detailed axial profile is more difficult to extract. This observation is attributed to the larger surface area of the structure (see Section 2.1), which increases the fraction of wall-adjacent regions. In these regions, MRI measurements are characterised by a reduced SNR due to partial-volume averaging, leading to a decreased detection accuracy. In general, the results may be affected by magnetic susceptibility differences between the two 3D-printed materials, particularly in gradient-echo imaging, where local field inhomogeneities can induce minor distortions or signal loss near surfaces. Minor registration errors cannot be excluded as a slight angular deviation of the experimental setup may have been present. Overall consistency between CAD and MRI can still be demonstrated. The additional optical inspection of the printed structures confirms that the additive manufacturing process is successful for all geometries and that the MRI data are valid.

3.2. Validation of velocity data

For quantitative evaluation of flow data, the MRI velocity data are validated by means of mass flow rate and divergence. The mass flow rate is calculated according to Eq. (3) across all slices and structures for the axial velocity. The comparison with measurements from the MFM is shown in Fig. 7. MRI-derived mass flow rates are averaged by arithmetic means over all slices.

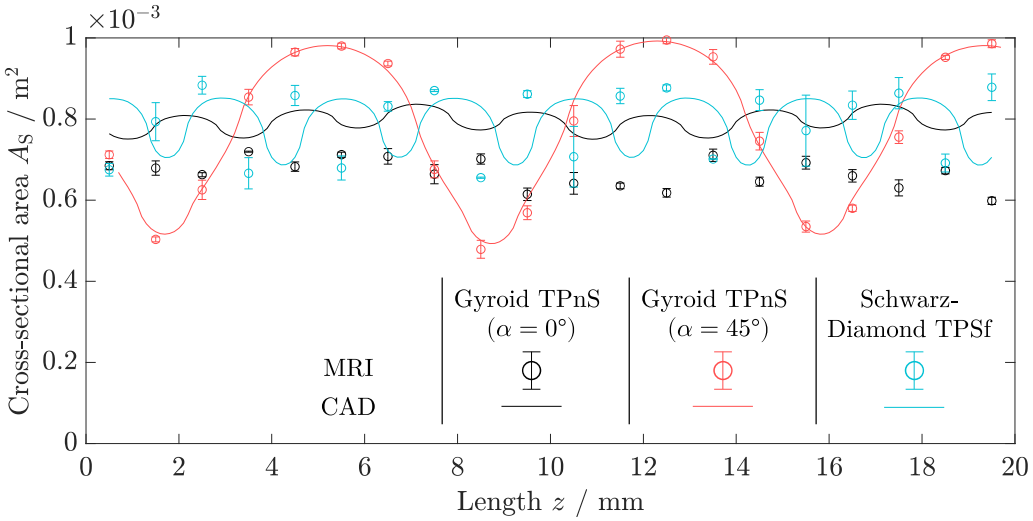

Fig. 6. Comparison of cross-sectional areas A_S derived from CAD and flow MRI data for the Gyroid TPnS structures ($\alpha = 0°$ and 45°) and the Schwarz-Diamond TPSf.

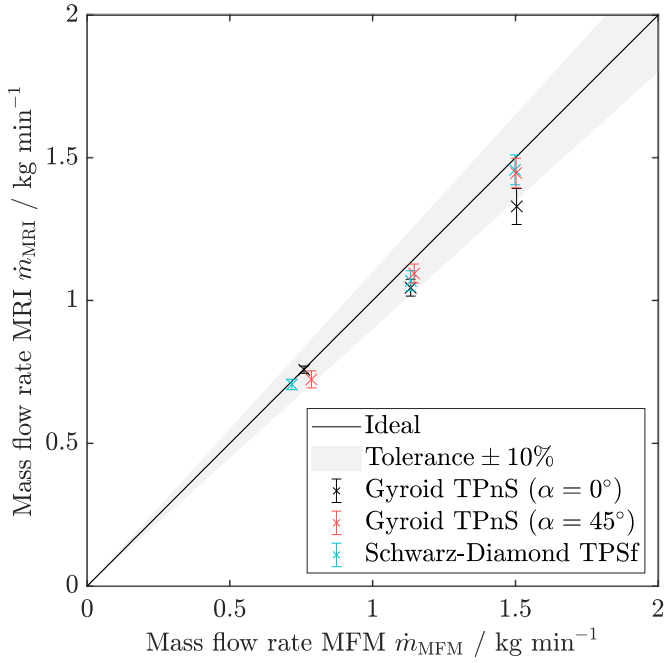

Fig. 7. Comparison of MRI-derived and measured mass flow rates of the Coriolis MFM, averaged across all slices.

On average, MRI underestimates the mass flow rate by 5.1 % compared to the reference values obtained from the MFM. The deviation increases with increasing flow rate. The maximum relative error is observed for the Gyroid TPnS ($\alpha = 0°$) at the highest flow rate, amounting to 12 %, with the MRI consistently underestimating the mass flow. This underestimation is consistent with previously reported MRI limitations, including partial-volume effects, phase dispersion within a voxel, which lead to phase cancellation and thus reduced measured velocities in the MRI data [74–76]. As discussed for structural integrity, magnetic susceptibility differences between the two 3D-printed materials may also affect the results here. The observed deviations are small enough to consider the MRI measurements quantitatively reliable for analysing flow behaviour within the investigated TPMS structures.

Table 4
Summary of the mean mass imbalance $\overline{\mathrm{div}_m\, \boldsymbol{u}}$ for all studied structures and operating points. The values are obtained by multiplying the mean slice divergence with the fluid density ρ and slice volume V_{Slice}, providing a measure of the global consistency of the MRI velocity fields.

Mass flow rate $\dot{M}$ / g min^{-1}	755	1150	1500
	Mean mass imbalance $\overline{\mathrm{div}_m\, \boldsymbol{u}}$ / g min^{-1}		
Gyroid TPnS ($\alpha = 0°$)	−8.9 ± 21.8	−1.4 ± 3.6	−6.8 ± 7.8
Gyroid TPnS ($\alpha = 45°$)	−4.3 ± 6.1	−0.33 ± 10.3	−5.4 ± 14.8
Schwarz-Diamond TPSf	−1.7 ± 28.4	1.9 ± 16.8	−1.1 ± 11.5

The analysis of the mass flow rate considers only the axial velocity w. Therefore, the lateral velocities u and v are not directly validated with the mass flow rate. To assess their accuracy, the divergence of the velocity field $\boldsymbol{u}$ is computed according to Eq. (4). Subsequently, a mean divergence value is determined for each entire slice and operating point. In this paper, all values denoted by an overline represent arithmetic means. The values are in the order of magnitude $\overline{\mathrm{div}\, \boldsymbol{u}} \lesssim 10^{-1}$ s^{-1} for all structures and operating points. To relate these values to the overall mass flow rate, each mean divergence is multiplied by the fluid density ρ and the slice volume $V_{Slice} = \frac{\pi}{4} D^2 L_{Slice} \epsilon$ (L_{Slice} = 1 mm), yielding the mass imbalance for the respective slice. Table 4 summarises the mean mass imbalance $\overline{\mathrm{div}_m\, \boldsymbol{u}}$, averaged over all pixels per slice and all slices for each operating point and structure. In this analysis, the standard error is used to quantify the uncertainty of the estimated mean.

As presented in Table 4, the mean mass imbalance remains small relative to the measured mass flow rate, with a relative error below 4 % for all cases. This confirms that the MRI-derived velocity fields are physically consistent, including the lateral velocity components. Furthermore, the divergence is independent of the operating conditions. The deviations are primarily caused by measurement noise. Furthermore, the slice thickness induces volumetric averaging effects, which intensify gradient variations in the MRI datasets, particularly in regions where the TPMS geometry varies within a single slice. Voxels intersecting solid boundaries can therefore produce artificially high local divergence values. Despite these effects, the global divergence analysis and its agreement with the measured mass flow rate confirm that the MRI velocity data are reliable and physically consistent, providing a reliable basis for further flow analysis.

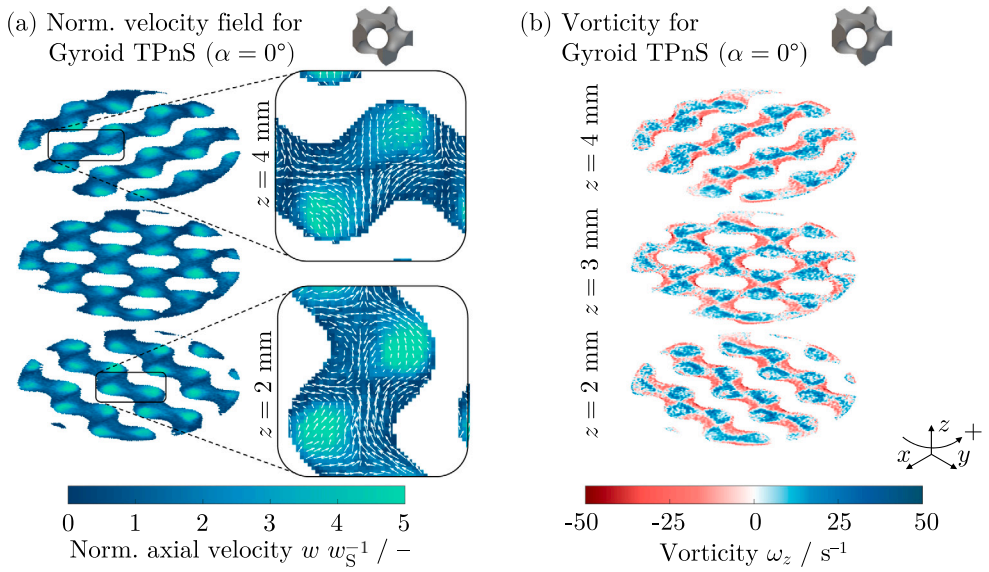

Fig. 8. MRI measurements are shown with in-plane velocity components u and v in the x- and y-directions are represented by arrows, while the colour scale indicates the axial velocity w, normalised by the superficial velocity w_S. Representative axial positions in (a). Corresponding vorticity fields ω_z in (b), representing rotation around the z-axis and calculated according to Eq. (5) for Gyroid TPnS ($\alpha = 0°$) at $Re_S = 156$.

3.3. Flow dynamics within TPMS structures

Following the validation of both the structural information and the flow data, the analysis now focuses on the flow behaviour within the TPMS structures. The structures are compared at similar Reynolds numbers, with the Gyroid TPnS examined at a Reynolds number of $Re_S \approx 156$ and the Schwarz-Diamond TPSf structure at $Re_S = 129$. Based on these Reynolds numbers, the flow conditions fall within Darcy-Forchheimer regime, where laminar and steady behaviour without vortices is expected [52]. Figs. 8(a) to 10(a) present three consecutive velocity fields at representative axial positions z measured by MRI velocimetry for the three TPMS structures. Arrows indicate the in-plane velocity components u and v in the x- and y-directions, while the colour scale represents the axial velocity w, normalised by the superficial fluid velocity w_S (see Table 1). In Figs. 8(b) to 10(b), the vorticity around the z-axis is shown, calculated according to Eq. (5).

The Gyroid TPnS ($\alpha = 0°$) (G) exhibits channelling behaviour, with axial velocities reaching five times the superficial velocity within the channels. This can be explained by the continuous channels running through the entire structure, generating high local channel velocities and a relative standard deviation of the axial velocity of (87 ± 6) %, which indicates a heterogeneous flow behaviour. Nevertheless, lateral flow structures are also observed. On average, the magnitudes of the lateral velocity components u_G and v_G correspond to (38 ± 4) % and (45 ± 4) %, respectively, of the mean axial velocity $\overline{w}_G$, indicating that the flow remains predominantly axial, despite noticeable lateral components. Characteristic helical flow structures arise as a direct consequence of the geometric features of the Gyroid TPnS ($\alpha = 0°$). Between adjacent channels, counter-rotating vortices develop in the negative coordinate direction. The positive vorticity consistently appears between two neighbouring channels, promoting transverse exchange and thereby enhancing local mass transfer. This behaviour is clearly visible in Fig. 8(b), where positive vorticity values of $\overline{\omega}^+_{z,\,G} = (12.3 \pm 0.6)\ s^{-1}$ and negative vorticity values of $\overline{\omega}^-_{z,\,G} = (-13.5 \pm 0.7)\ s^{-1}$ are observed. The nearly equal magnitudes of the positive and negative mean vorticities $\left(|\overline{\omega}^+_{z,\,G}| \approx |\overline{\omega}^-_{z,\,G}|\right)$ indicate the presence of symmetric, counter-rotating helical flow structures. Such flow patterns have also been reported in the literature and are in good agreement with the present findings [10,43]. However, although lateral velocity components are present, the overall flow is still dominated by pronounced channelling behaviour. Such a flow pattern is generally undesirable for chemical reactor applications, as it leads to non-uniform mass and heat transfer, potentially reducing reaction selectivity and total efficiency.

In order to overcome these challenges, the rotated Gyroid TPnS structure is studied. The tilt misaligns the channels with the main flow direction, effectively reducing channelling while preserving the overall geometry and volume-specific surface area of the unit cell. In contrast to the unrotated configuration, the 45°-rotated Gyroid TPnS exhibits a different flow pattern, characterised by the absence of localised high-velocity regions. However, the overall level of flow heterogeneity remains comparable to the axial velocity standard deviation of (84 ± 26) %. A closer inspection reveals that, in contrast to the unrotated Gyroid, the rotated configuration exhibits a pronounced axial dependence of the velocity standard deviation. For individual slices, velocity standard deviations of 43 % are observed (e.g. at z = 1 mm in Fig. 9(a)), indicating a locally more homogeneous flow profile. In contrast, other axial positions exhibit higher values, reaching 76 % and 105 % at z = 2 mm and z = 3 mm, respectively. Unlike the unrotated Gyroid TPnS, the high velocity standard deviations observed in the rotated configuration are associated with regions of low velocities, as illustrated by the close-up in Fig. 9(a) at z = 2 mm. The observed fluctuations in the velocity distribution are associated with the strong axial variation of the free cross-sectional area along the structure (see Fig. 6).

The mean axial velocity reaches approximately $\overline{w}_{G45}\ w_S^{-1} = 1.5 \pm 0.4$, while the lateral velocity components account for (49 ± 9.4) % and (52 ± 12) % of the mean axial velocity in the x- and y-directions, respectively. This represents an increase compared to the unrotated case. As seen in Fig. 9(a), at z = 2 mm, counter-rotating lateral flow structures emerge within the main channels. This behaviour is further reflected in the vorticity distribution shown in Fig. 9(b), where alternating positive and negative vorticity regions are observed across the cross-section, with mean values for whole FOV of $\overline{\omega}^+_{z,\,G45} = (12.2 \pm 1.0)\ s^{-1}$ and $\overline{\omega}^-_{z,\,G45} = (-12.5 \pm 1.3)\ s^{-1}$, indicative of symmetric, counter-rotating vortical motion.

Overall, these changes indicate that unit-cell rotation redistributes the axial flow and promotes locally more homogeneous flow regions. A more homogeneous flow field is generally associated with enhanced heat and mass transfer [77]. Accordingly, the Gyroid TPnS ($\alpha = 45°$) may promote improved heat and mass transfer performance by inducing locally more homogeneous flow conditions and a more uniform

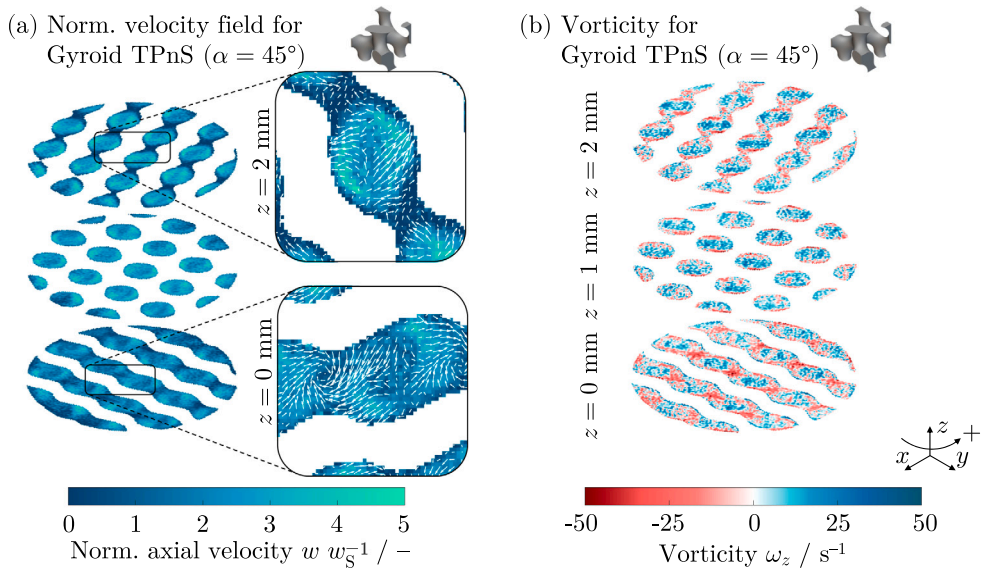

Fig. 9. MRI measurements are shown with in-plane velocity components u and v in the x- and y-directions are represented by arrows, while the colour scale indicates the axial velocity w, normalised by the superficial velocity w_S. Representative axial positions in (a). Corresponding vorticity fields ω_z in (b), representing rotation around the z-axis and calculated according to Eq. (5) for Gyroid TPnS ($\alpha = 45°$) at $Re_S = 155$.

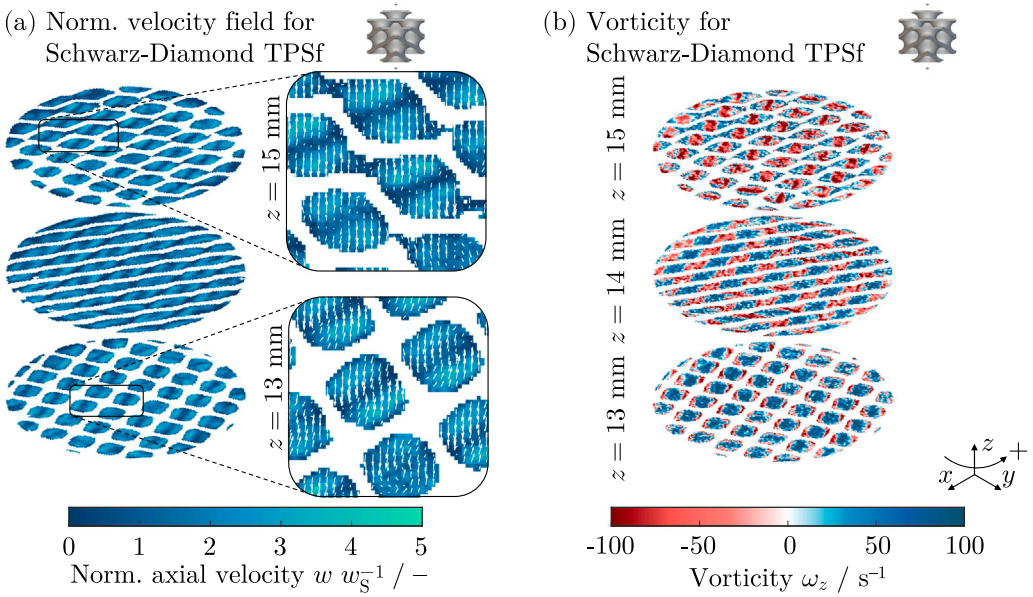

Fig. 10. MRI measurements are shown with in-plane velocity components u and v in the x- and y-directions are represented by arrows, while the colour scale indicates the axial velocity w, normalised by the superficial velocity w_S. Representative axial positions in (a). Corresponding vorticity fields ω_z in (b), representing rotation around the z-axis and calculated according to Eq. (5) for Schwarz-Diamond TPSf at $Re_S = 129$.

distribution of reactants. This effect arises from the suppression of channelling throughout the structure and the increase in the magnitude of lateral velocities, which facilitate enhanced transverse transport, despite comparable global flow heterogeneity. Finally, the present results complement prior numerical studies on rotated TPMS unit cells by showing that such orientation effects also appear in realistic additively manufactured structures [32].

The Schwarz-Diamond TPSf (SD) structure exhibits a larger volume-specific surface area and a smaller hydraulic diameter compared to the Gyroid TPnS (see Section 2.2). Consequently, for an equivalent Reynolds number, a higher mass flow rate is required within the structure. In the Schwarz-Diamond TPSf geometry, some isolated gas bubbles could not be avoided, as indicated by the region of reduced signal intensity on the left-hand side of the TPMS structure in Fig. 10(a) at $z = 14$ mm. However, their influence on the flow is expected to be negligible, since the bubbles are small compared to the channel cross-section and occur only irregularly. Fig. 10(a) illustrates the corresponding flow field, revealing an even more homogeneous velocity distribution, with a mean normalised axial velocity at $\overline{w}_{SD}\ w_S^{-1} = 1.4 \pm 0.2$ across all slices. The fraction of axial velocities exceeding $3w_S$ serves as another indicator of flow homogenisation. For the Gyroid TPnS ($\alpha = 0°$), (21 ± 2) % of the axial velocities lie above this threshold, whereas the rotated configuration reduces this fraction to (11 ± 7) %, and the Schwarz-Diamond TPSf to only (4.4 ± 1.3) %. This progression reflects the increasingly uniform velocity distribution across the three geometries.

A closer examination of a single cell in the Schwarz-Diamond TPSf structure shows that the flow separates or merges in the centre due to locally reduced axial velocities. The velocity measurements further

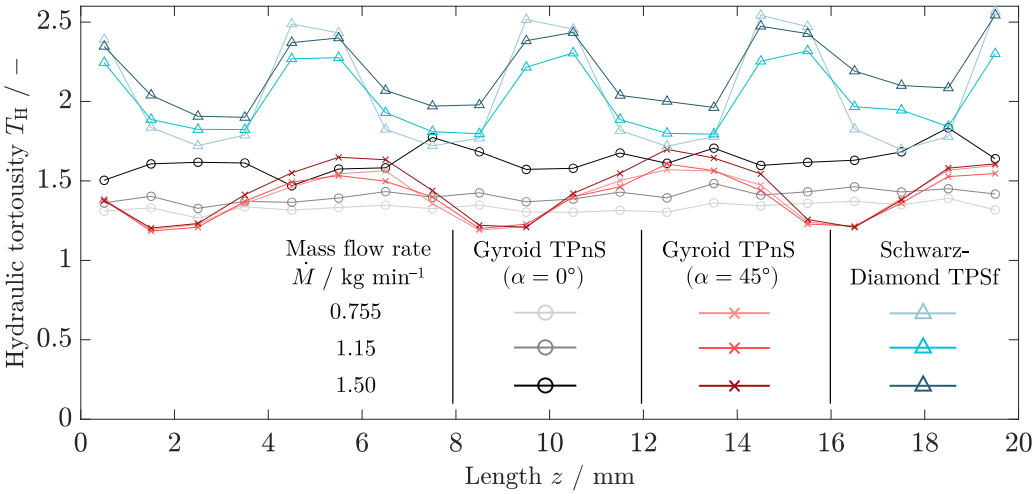

Fig. 11. Hydraulic tortuosity T_h for the three TPMS structures (Gyroid TPnS, rotated Gyroid TPnS, and Schwarz-Diamond TPSf) at different Reynolds numbers based on MRI velocimetry. The tortuosity quantifies the ratio of radial to axial velocity components (see Eq. (6)), providing a measure of the degree of lateral flow and mixing intensity.

indicate that at $z = 13$ mm, the lateral velocity components are directed towards each other, whereas at $z = 15$ mm, they diverge. This alternating behaviour forms the characteristic merge-split flow pattern, which has been described in the literature as particularly beneficial for enhancing mixing and transport processes [10]. As shown in Fig. 10(b), the slice at $z = 13$ mm reveals that each individual channel exhibits a positive vorticity in the centre, while a negative vorticity forms at the channel boundaries. In the subsequent axial slice, the channels merge into an elongated longitudinal passage, giving rise to alternating regions of positive and negative vorticity. At $z = 15$ mm where the flow again separates into distinct channels, the vorticity pattern is reversed compared to the slice at $z = 13$ mm. The Schwarz-Diamond TPSf exhibits vorticity magnitudes higher than those of the Gyroid TPnS structures, with mean values of $\overline{\omega}^{+}_{z,\,\mathrm{SD}} = (62.7 \pm 4.4)\ \mathrm{s}^{-1}$ and $\overline{\omega}^{-}_{z,\,\mathrm{SD}} = (-65.1 \pm 3.8)\ \mathrm{s}^{-1}$. This pronounced merge-split behaviour, together with elevated vorticity levels, is advantageous for chemical engineering applications, as it is indicative of enhanced cross-mixing and improved homogenisation of reactants.

Following the analysis of local flow features, global flow quantities are evaluated. To further quantify the degree of lateral flow and mixing intensity, the hydraulic tortuosity, calculated according to Eq. (6), is evaluated for all three TPMS geometries and operating conditions (see Fig. 11). The Schwarz-Diamond TPSf exhibits mean values 46 % higher than those of the Gyroid TPnS structures, indicating a stronger cross-flow motion. For the Schwarz-Diamond TPSf, a mean hydraulic tortuosity of $\overline{T}_{\mathrm{h,\,SD}} = 2.10 \pm 0.25$ is obtained, whereas the Gyroid TPnS and rotated Gyroid TPnS show comparable magnitudes $\left(\overline{T}_{\mathrm{h,\,G}} = 1.46 \pm 0.053 \text{ and } \overline{T}_{\mathrm{h,\,G45}} = 1.42 \pm 0.16\right)$. The Gyroid TPnS reveals a moderate increase in hydraulic tortuosity with Reynolds number, rising by about 23 % for a 100 % increase in Re_S. Axial variations of the hydraulic tortuosity remain below 5 %, reflecting the nearly constant cross-sectional area and strong influence of channelling throughout the whole structure. By contrast, the rotated Gyroid TPnS exhibits stronger axial fluctuations of 11 %, consistent with its pronounced variation in free cross-sectional area (see Fig. 6). In comparison, the Schwarz-Diamond TPSf shows variations of hydraulic tortuosity of 12 %, which can be attributed to its non-continuous channels and intricate geometry that promote enhanced lateral mixing through merge-split patterns. Clarke et al. [27] reported $T_h = 1.32$ for the Schwarz-Diamond TPSf structure under creeping and inertial flow conditions in smaller-scale systems. Compared to their findings, the present study shows by 59 % higher hydraulic tortuosity values, consistent with the expected increase of lateral mixing at higher Reynolds numbers.

3.4. Cross-validation of MRI and CFD results

The velocity fields obtained from MRI are compared with those from CFD simulations. CFD is employed here for cross-validation of the MRI data, while the MRI measurements simultaneously provide experimental validation of the numerically retrieved velocity fields. Although MRI and CFD data can be obtained for all three structures, the CFD-MRI comparison is performed on the Gyroid TPnS ($\alpha = 0°$) structure, exemplary. This structure is selected because it exhibits pronounced channelling behaviour and the highest local velocities, representing challenging conditions for MRI flow measurements due to rapid spatial velocity variations. The Gyroid TPnS ($\alpha = 45°$) and Schwarz-Diamond TPSf structures exhibit more homogeneous flow behaviour. Notably, the Schwarz-Diamond TPSf structure exhibits a smaller hydraulic diameter, which represent a different challenge for both MRI measurements and CFD simulations. However, the present analysis focuses on the unrotated Gyroid TPnS structure, while the complete corresponding MRI data for all cases are provided in [69].

The CFD data possess a 2.7-fold higher spatial resolution, highlighting the necessity of both methods. As explained in Section 2.5, the computational grid cannot be adapted to the lower spatial resolution of the MRI data due to the requirements of grid independence. At coarser grid resolutions, no accurate solution of the momentum equations can be obtained. Therefore, the CFD simulations are performed on a grid-independent mesh, and the results are subsequently mapped to the MRI resolution during post-processing using scattered data interpolation and linear interpolation. The detailed procedure used to align both datasets is described in Section 2.5.

A qualitative comparison of the axial velocity is shown in Fig. 12 for three consecutive slice pairs of the Gyroid TPnS ($\alpha = 0°$) at $Re_S = 156$. These data illustrate the close correspondence between the CFD and MRI results. The characteristic channels for the axial velocity of the Gyroid TPnS structures are clearly visible in both datasets, appearing at identical spatial locations and exhibiting comparable shapes and velocity magnitudes. Regions of low velocity, which are visible as horizontally aligned zones in the slice pair at $z = 2$ mm, are likewise reproduced in both CFD and MRI results. Analysis of subsequent slice pairs confirms this consistency, indicating that both methods capture the same geometric and hydrodynamic features of the structure. Minor discrepancies occur near the wall regions, as illustrated by the red regions in Fig. 12. These are particularly evident within $(x, y) \in (15\ \mathrm{mm} \le x \le 20\ \mathrm{mm},\ -10\ \mathrm{mm} \le y \le 10\ \mathrm{mm};\ -20\ \mathrm{mm} \le x \le -15\ \mathrm{mm},\ -10\ \mathrm{mm} \le y \le 10\ \mathrm{mm})$, where the MRI signal intensity is

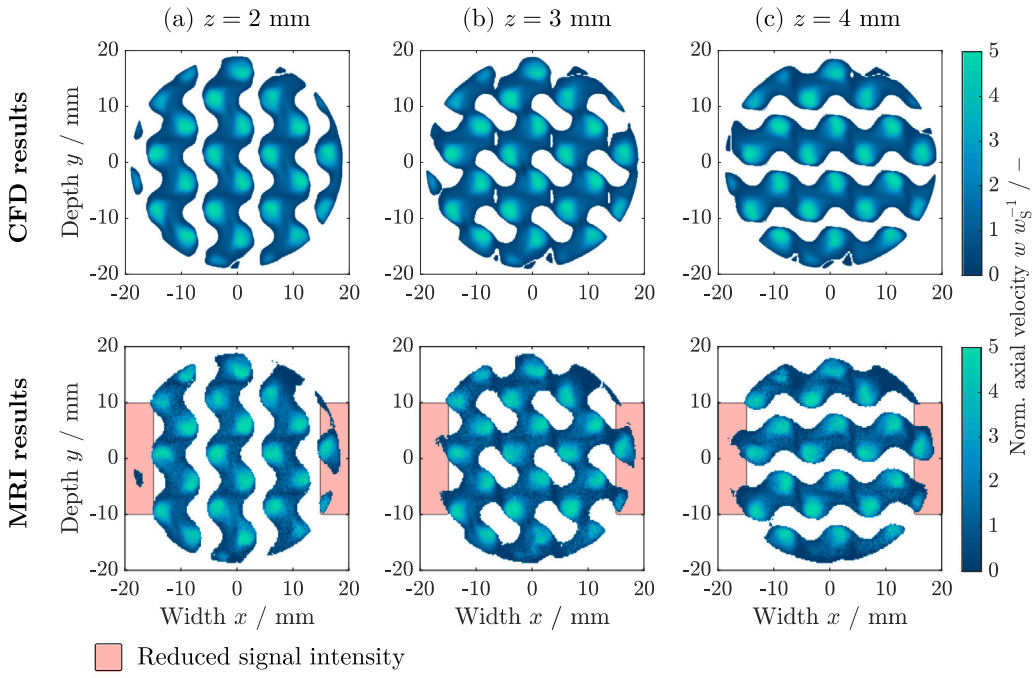

Fig. 12. Qualitative comparison of MRI and CFD velocity fields for Gyroid TPnS (α = 0°) at Re_S = 156. Axial velocity fields are normalised by superficial velocity w_S. The CFD data are volumetrically averaged over a slice thickness of 1 mm to match the MRI spatial resolution. The red region indicates reduced MRI signal intensity due to the RF coil position.

reduced due to the RF coil position at $(x, y) \in [-20\text{ mm}, -10\text{ mm}]$. This position results in high signal intensity along the cross-sectional diagonal, while regions further away from the RF coil exhibit weaker signals. The local signal intensity distribution shown in Fig. 13 confirms this effect, indicating that the observed deviations originate from RF receive coil positioning rather than inaccuracies in the CFD data or the additive manufacturing process. Moreover, both MRI and CFD capture the three-dimensional velocity fields. To further illustrate this, a full three-dimensional visualisation of the lateral velocity components is provided in the supplementary material. Characteristic minima and maxima of lateral velocities are identified at the same spatial locations in both datasets, demonstrating clear qualitative agreement between MRI and CFD.

To assess the influence of the Reynolds number, additional consecutive slice pairs for all velocity components at the remaining operating conditions Re_S = 237 and Re_S = 310 are provided in the supplementary material to facilitate a three-dimensional assessment of the velocity fields. As a representative example, Fig. 14 presents the slice at z = 2 mm for the three operating points considered.

Overall, all datasets demonstrate strong agreement between CFD and MRI. However, the SNR is observed to decrease with increasing volumetric flux at the higher local velocities in the channels of the non-rotated Gyroid TPnS. As discussed in Section 2.3, the VENC is adjusted for each condition to avoid phase wrapping while maintaining sensitivity. Thus, although phase contrast improves, the precision of velocity estimation is still be compromised by reduced magnitude SNR. This interplay between magnitude SNR, VNR, VENC adjustment, and phase contrast has been intensively studied in previous MRI flow studies [63–65]. The MRI data at Re_S = 237 remain of sufficient quality for reliable velocity estimation, while the SNR decreases significantly at Re_S = 310 for all three velocity components. This behaviour may arise from the onset of vortex formation around $Re_S \approx 250$, resulting in a flow increasingly dominated by unsteady behaviour [52,53]. Unsteady, transitional flow, which cause signal ghosts and motion artefacts in all phase-encoding directions, are also influencing the measurement unfavourably. The unsteady nature of the flow leads to heterogeneous

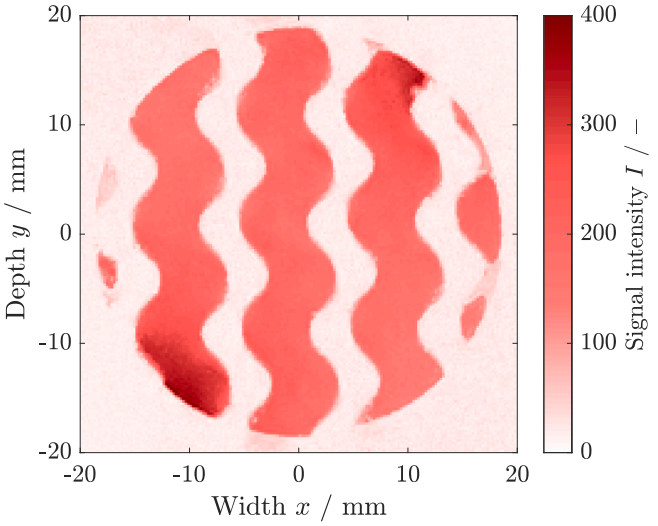

Fig. 13. Local MRI signal intensity distribution of the Gyroid TPnS (α = 0°) at Re_S = 156, illustrating reduced signal intensity near the walls, particularly in regions farther from the RF coil, shown exemplarily at z = 2 mm.

velocities within individual voxels, causing additional signal attenuation [78]. A more detailed investigation of these effects is beyond the scope of the present work. However, previous studies have explored the characterisation of unsteady and turbulent flow features, particularly at higher Reynolds numbers [29,79].

In addition to qualitative assessment, a quantitative comparison is essential to verify that the MRI not only reproduces the flow patterns but also accurately captures the corresponding velocity magnitudes. For this purpose, a pixel-wise comparison between the CFD and MRI datasets is performed. Since the MRI measurements feature a lower

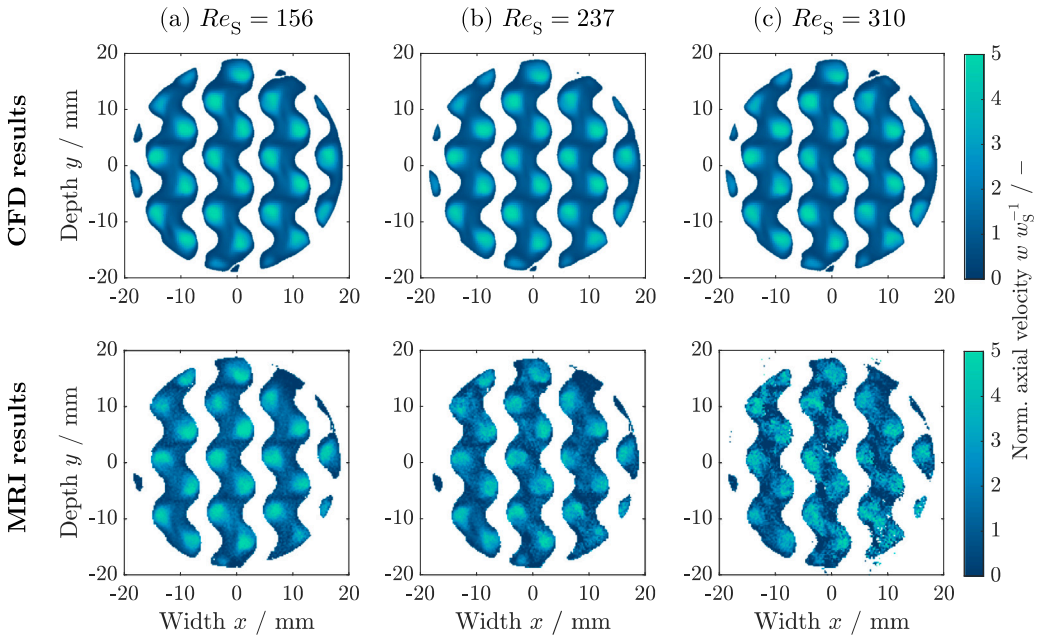

Fig. 14. Qualitative comparison of MRI- and CFD-derived velocity fields for the Gyroid TPnS (α = 0°) at Re_S = 156 (a), Re_S = 237 (b), and Re_S = 310 (c) at z = 2 mm. The axial velocity fields are normalised by the superficial velocity w_S.

spatial resolution than the CFD data, the CFD velocity fields are interpolated to match the MRI resolution prior to comparison. The relative Root Mean Square Error (rRMSE) deviation of the axial velocity, $w_{dev}(x, y)$, is then evaluated for each in-plane location x, y according to

$$w_{dev}(x,y) = \sqrt{\frac{\left(w_{MRI}(x,y) - w_{CFD}(x,y)\right)^2}{(\overline{w}_{MRI,\ CFD})^2(x,y)}}\ . \tag{10}$$

Here, $w_{MRI}(x, y)$ and $w_{CFD}(x, y)$ denote the local axial velocities obtained from MRI and CFD, respectively, while $\overline{w}_{MRI,CFD}(x, y)$ represents their local mean value [27,29]. An example of this comparison is illustrated in Fig. 15(a) for the MRI/ CFD slice pair (z = 2 mm) shown in Fig. 12(a). An examination of Fig. 15(a) shows that in regions where the CFD and MRI data overlap, mean rRMSE deviations of $\overline{w}_{dev}$ = 40 % are observed between the two datasets at z = 2 mm. For Re_S = 237 and Re_S = 310, the deviations amount to $\overline{w}_{dev}$ = 49 % and $\overline{w}_{dev}$ = 73 %, respectively (see supplementary material for the corresponding quantitative comparisons). The mean rRMSE $\overline{w}_{dev}$ is calculated as the square root of the ratio of the separately summed numerator and denominator terms of Eq. (10). Reasons for the deviation are system-related imperfections, such as minor gas bubbles, local variations in the printing quality of additively manufactured structures, and residual registration inaccuracies between the MRI and CFD datasets.

In addition, the decrease in SNR with distance from the RF coil may contribute to the observed deviations. Additional sources of noise is another contributing factor. Near-wall regions, where partial-volume effects and signal loss lead to an under-representation of velocities within approximately 500 µm of the solid boundaries. Despite the good qualitative agreement, the quantitative discrepancies remain high, particularly at elevated Reynolds numbers, where the flow becomes increasingly unsteady, amplifying local velocity fluctuations and measurement uncertainties. Pixel-wise comparisons are more sensitive, as they capture local discrepancies at the resolution limit of the MRI system. In addition, small misalignments, local velocity fluctuations, and regions of low or near-zero flow may further amplify relative deviations, despite an accurate representation of the macroscopic flow features.

Thus, Fig. 15(b) shows the normalised axial velocity profiles for two representative positions of constant width x. The selected x-positions correspond to locations where transitions between structural elements and flow regions occur. The graph shows relative deviations of 10 % and 14 % at x = 2 mm and x = 12 mm, respectively. Relative deviations between CFD and MRI data are computed element-wise. Cases where both values are zero are set to 0 %, while divisions by zero are treated as undefined. The mean relative deviation is then calculated using only values below the 95th percentile to mitigate the influence of outliers. These values indicate a strong agreement between CFD and MRI. Close to the pipe wall, detection becomes increasingly unreliable, leading to larger deviations. Consequently, the CFD simulations are cross-validated using direct comparison with the MRI measurements. Thus, CFD can act complementary to resolve fine-scale flow details in regions that are difficult to access experimentally, particularly near the walls and at higher Reynolds numbers. Despite these limitations, the overall agreement between CFD and MRI is strong, enabling cross-validation of both techniques.

4. Conclusion and outlook

The flow behaviour in additively manufactured TPMS structures is studied using a large-bore vertical 3 T MRI system. Cross-validation between the experimental data and the numerical simulations is performed. Three different TPMS structures are analysed under Darcy-Forchheimer regime. The experimental setup enables quantitative flow measurements in TPMS geometries with a diameter of 38 mm and lengths of up to 1000 mm, thereby extending the accessible spatial scales compared to conventional horizontally orientated MRI systems.

Structural integrity is verified, and reliable velocity acquisition is ensured through mass-flow-rate validation with mean deviations of 5.1 %. Furthermore, the MRI system provides fully three-dimensional velocity fields with a relative mass divergence deviation below 4 %, demonstrating the physical consistency of the measurements.

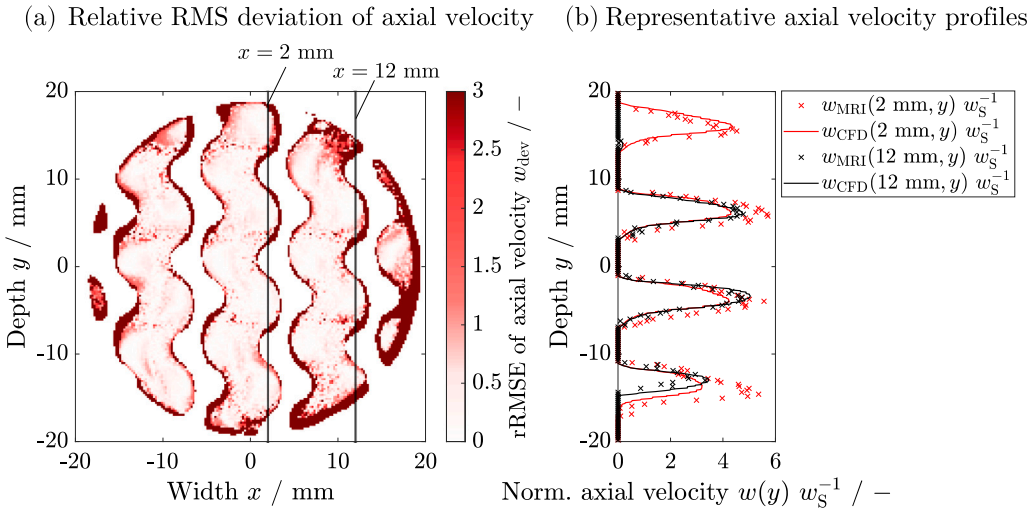

Fig. 15. Pixel-wise comparison of the axial velocity from CFD and MRI for the slice pair with Gyroid TPnS ($\alpha = 0°$) at $z = 2$ mm and $Re_{\mathrm{S}} = 156$, showing the rRMSE deviation of the axial velocity in (a). In (b), two representative velocity profiles at fixed x-positions are presented.

The MRI measurements reveal that the studied structures exhibit different flow features. The unrotated Gyroid TPnS exhibits pronounced channelling due to continuous flow pathways, resulting in strong axial velocity dominance even though lateral velocity components reach approximately 42 % of the axial mean. After rotating the unit cell, redistributes the axial flow and promotes locally more homogeneous flow regions, which is advantageous for chemical engineering applications. This demonstrates that future design of TPMS structures must account not only for the choice of unit cell but also for its orientation. The Schwarz-Diamond TPSf exhibits pronounced merge-split behaviour and shows the highest potential for chemical engineering applications, with a 46 % increase in lateral mixing compared to the Gyroid TPnS structures.

Validation of numerical simulations and cross-validation of MRI data are performed. CFD velocity fields match MRI velocity fields quantitatively and qualitatively. Pixel-wise comparisons show good agreement in Darcy-Forchheimer regime with deviation of 40 %. The resulting CFD-MRI agreement confirms the fidelity of the experimental measurements and the suitability of the CFD framework for resolving finer-scale flow structures.

The combined experimental-numerical approach provides a foundation for future analysis of heat and mass transfer. By enabling spatially resolved characterisation of flow behaviour in complex TPMS reactor geometries, this work directly contributes to the SMART Reactors objective of reliably characterising transport processes in adaptive reactor systems. Future MRI developments are expected to enable the direct observation of chemical reactions, including the mapping of temperature and chemical composition within structured reactors [80,81]. The flow-field characterisation presented forms a basis for these future studies. Beyond the present configuration, the vertical MRI system can accommodate larger experimental setups. With a bore diameter of 400 mm, studies at industrially relevant scales become feasible, although further development of multi-channel detection systems will be required to maintain spatial and temporal resolution at larger column diameters.

CRediT authorship contribution statement

Timo Merbach: Writing – review & editing, Writing – original draft, Investigation, Formal analysis, Data curation, Conceptualization. **Muhammad Adrian:** Writing – review & editing, Writing – original draft, Investigation, Formal analysis, Data curation, Conceptualization. **Christoph Wigger:** Writing – review & editing, Writing – original draft, Formal analysis, Data curation, Conceptualization. **Selma Iraqi Houssaini:** Writing – review & editing, Investigation, Conceptualization. **Benedict Bayer:** Writing – review & editing, Investigation, Formal analysis, Data curation, Conceptualization. **Artyom Tsanda:** Writing – review & editing, Investigation, Formal analysis, Data curation, Conceptualization. **Serhan Acikgöz:** Writing – review & editing, Conceptualization. **Christian Weiland:** Writing – review & editing, Conceptualization. **Felix Kexel:** Writing – review & editing, Conceptualization. **Dirk Herzog:** Writing – review & editing, Funding acquisition, Conceptualization. **Marko Hoffmann:** Writing – review & editing, Funding acquisition, Conceptualization. **Ingomar Kelbassa:** Writing – review & editing, Funding acquisition, Conceptualization. **Tobias Knopp:** Writing – review & editing, Funding acquisition, Conceptualization. **Alexander Penn:** Writing – review & editing, Funding acquisition, Conceptualization. **Michael Schlüter:** Writing – review & editing, Funding acquisition, Conceptualization.

Declaration of Generative AI and AI-assisted technologies in the writing process

During the preparation of this work the authors used ChatGPT-4o in order to improve clarity and readability. The authors have thoroughly checked all the proposed edits and take full responsibility for the content of this manuscript.

Declaration of competing interest

The authors declare that they have no known competing financial interests or personal relationships that could have appeared to influence the work reported in this paper.

Acknowledgements

We thank Prof. Wilhelm Schwieger (FAU Erlangen-Nürnberg) for the valuable discussions on the results and for suggesting the idea of rotating the Gyroid TPnS unit cell. Publishing fees supported by Funding Program Open Access Publishing of Hamburg University of Technology (TUHH). The Magnetic Resonance Imaging System (large-bore 3 T vertical MRI system) was funded by the Deutsche Forschungsgemeinschaft (DFG, German Research Foundation), Germany – project number 422037415 – under the “Major Research Instrumentation”

funding program according to Art. 91b of the Basic Law (GG) and by The Free and Hanseatic City of Hamburg. This project is funded by the Deutsche Forschungsgemeinschaft (DFG, German Research Foundation), Germany – SFB 1615 – 503850735. The authors gratefully acknowledge this funding.

Appendix A. Nomenclature

Roman symbols	
A	Area / m^2
A_P	Pixel area / m^2
A_S	Cross-sectional area / m^2
$A_{W,\,S}$	Wetted surface area / m^2
a	Volume-specific surface area / $m^2\ m^{-3}$
c	Concentration / mol L^{-1}
D	Pipe diameter / m
D_h	Hydraulic diameter / m
d_{50}	Median particle diameter / m
div $\boldsymbol{u}$	Divergence of the velocity field $\boldsymbol{u}$ / s^{-1}
$\mathrm{div}_m\ \boldsymbol{u}$	Mass imbalance of the velocity field $\boldsymbol{u}$ / kg s^{-1}
F	Frequency / –
F_S	Safety factor / –
f_i	Numerical solution on grid level i / –
g	Gravitational acceleration / m s^{-2}
h	Average mesh size / m
I	Signal intensity / –
L_E	Entrance length / m
$L_{E,\,M}$	Entrance length of TPMS structures / m
L_M	Module length / m
L_{Slice}	Slice length / m
$\dot{M}$	Mass flow rate / kg s^{-1}
n	Number of pixels / –
p	Pressure / Pa
Δp	Pressure drop / Pa
P	Convergence index / –
R^*	Grid resolution / –
r	Refinement factor / –
T	Temperature / K
T_h	Hydraulic tortuosity / –
T_1	Longitudinal relaxation time / s
V_W	Wetted volume / m^3
$\boldsymbol{u}$	Vector of velocity field / m s^{-1}
u	Lateral velocity in x-direction / m s^{-1}
v	Lateral velocity in y-direction / m s^{-1}
w	Axial velocity / m s^{-1}
w_{dev}	Relative root mean square error deviation / –
w_S	Superficial velocity / m s^{-1}
Δx	Distance between nodes in x / m
Δy	Distance between nodes in y / m
Δz	Distance between nodes in z / m
x	Width / m
y	Depth / m
z	Length / m
Greek symbols	
α	Rotation angle / °
η	Viscosity / Pa s
ϵ	Porosity / –
ϵ	Change of the numerical solution / –
ρ	Density / kg m^{-3}
ω_z	Vorticity around z-axis / s^{-1}
ω_z^+	Positive vorticity around z-axis / s^{-1}
ω_z^-	Negative vorticity around z-axis / s^{-1}
Dimensionless numbers	
Re_S	Reynolds number for porous media

Abbreviations	
CAD	Computer-Aided Design
CFD	Computational Fluid Dynamics
ECT	Electrical Capacitance Tomography
ECVT	Electrical Capacitance Volume Tomography
FOV	Field Of View
G	Gyroid TPnS ($\alpha = 0°$)
G45	Gyroid TPnS ($\alpha = 45°$)
GCI	Grid Convergence Index
M2D	Multi-two-Dimensional
MFM	Mass Flow Meter
MRI	Magnetic Resonance Imaging
NMR	Nuclear Magnetic Resonance
PBF-LB/P	Laser-Based Powder Bed Fusion of Polymers
PIV	Particle Image Velocimetry
PTV	Particle Tracking Velocimetry
QFlow	QuantitativeFlow
RF	Radio Frequency
rRMSE	relative Root Mean Square Error
SD	Schwarz-Diamond TPSf
SLA	Stereolithography
SLS	Selective Laser Sintering
SNR	Signal-to-Noise-Ratio
TPMS	Triply Periodic Minimal Surface
TPnS	Triply Periodic endo-Skeleton
TPSf	Triply Periodic Surface
TPxS	Triply Periodic exo-Skeleton
VENC	Velocity Encoding
VNR	Velocity-to-Noise-Ratio
VPP-UVL	Vat Photopolymerisation by Ultra Violet Laser beam

Appendix B. Supplementary data

Supplementary material related to this article can be found online at https://doi.org/10.1016/j.cej.2026.176536.

Data availability

The data that support the findings of this study are openly available at the following URL/DOI: https://doi.org/10.15480/882.16072.

References

[1] A. Cybulski, J.A. Moulijn, Structured Catalysts and Reactors, CRC Press, 2005, http://dx.doi.org/10.1201/9781420028003.

[2] K. Pangarkar, T.J. Schildhauer, J.R. van Ommen, J. Nijenhuis, F. Kapteijn, J.A. Moulijn, Structured packings for multiphase catalytic reactors, Ind. Eng. Chem. Res. 47 (10) (2008) 3720–3751, http://dx.doi.org/10.1021/ie800067r.

[3] F. Kapteijn, J.A. Moulijn, Structured catalysts and reactors – Perspectives for demanding applications, Catal. Today 383 (2022) 5–14, http://dx.doi.org/10.1016/j.cattod.2020.09.026.

[4] L. Fratalocchi, G. Groppi, C.G. Visconti, L. Lietti, E. Tronconi, Packed-POCS with skin: A novel concept for the intensification of non-adiabatic catalytic processes demonstrated in the case of the Fischer-Tropsch synthesis, Catal. Today 383 (2022) 15–20, http://dx.doi.org/10.1016/j.cattod.2020.12.031.

[5] J. Feng, J. Fu, X. Yao, Y. He, Triply periodic minimal surface (TPMS) porous structures: from multi-scale design, precise additive manufacturing to multi-disciplinary applications, Int. J. Extrem. Manuf. 4 (2) (2022) 022001, http://dx.doi.org/10.1088/2631-7990/ac5be6.

[6] L. Eckendörfer, D. Rudolf, A. Brix, M. Börnhorst, H. Freund, Periodic open cellular structures in chemical engineering: Application in catalysis and separation processes, Annu. Rev. Chem. Biomol. Eng. 15 (1) (2024) 163–186, http://dx.doi.org/10.1146/annurev-chembioeng-101121-085630.

[7] H. Bai, J. Theuerkauf, P.A. Gillis, P.M. Witt, A coupled DEM and CFD simulation of flow field and pressure drop in fixed bed reactor with randomly packed catalyst particles, Ind. Eng. Chem. Res. 48 (8) (2009) 4060–4074, http://dx.doi.org/10.1021/ie801548h.

[8] F.M. Baena-Moreno, M. Gonzalez-Castano, J.C. Navarro de Miguel, K.U. Miah, R. Ossenbrink, J.A. Odriozola, H. Arellano-Garcia, Stepping toward efficient microreactors for CO2 methanation: 3D-printed Gyroid geometry, ACS Sustain. Chem. Eng. 9 (24) (2021) 8198–8206, http://dx.doi.org/10.1021/acssuschemeng.1c01980.

[9] J. Feng, J. Fu, C. Shang, Z. Lin, B. Li, Porous scaffold design by solid T-splines and triply periodic minimal surfaces, Comput. Methods Appl. Mech. Engrg. 336 (2018) 333–352, http://dx.doi.org/10.1016/j.cma.2018.03.007.

[10] M.G. Gado, O. Al-Ketan, M. Aziz, R.A. Al-Rub, S. Ookawara, Triply periodic minimal surface structures: Design, fabrication, 3D printing techniques, state-of-the-art studies, and prospective thermal applications for efficient energy utilization, Energy Technol. 12 (5) (2024) 2301287, http://dx.doi.org/10.1002/ente.202301287.

[11] S. Acikgöz, C. Wigger, T. Merbach, F. Kexel, M.I. Maiwald, D. Herzog, I. Kelbassa, M. Schlüter, Design guidelines for laser powder bed fusion of triply periodic minimal surface structures for applications in smart reactors, Prog. Addit. Manuf. (2026) http://dx.doi.org/10.1007/s40964-025-01457-y.

[12] B. Reynolds, F. Lecarpentier, D. Holland, Heat transfer and topological characterisation of TPMS structures using 3D printed materials, Int. J. Heat Mass Transfer 245 (2025) 126992, http://dx.doi.org/10.1016/j.ijheatmasstransfer.2025.126992.

[13] M.A. Northrup, T.J. Kulp, S.M. Angel, Fluorescent particle image velocimetry: application to flow measurement in refractive index-matched porous media, Appl. Opt. 30 (21) (1991) 3034–3040, http://dx.doi.org/10.1364/AO.30.003034.

[14] D. Sen, D.S. Nobes, S.K. Mitra, Optical measurement of pore scale velocity field inside microporous media, Microfluid. Nanofluidics 12 (1) (2012) 189–200, http://dx.doi.org/10.1007/s10404-011-0862-x.

[15] J. Li, Y. Yang, X. Zhu, D. Ye, R. Chen, Q. Liao, Visual depiction and numerical characterization of intricate flow in triply periodic minimal surface foams, Phys. Fluids 36 (8) (2024) http://dx.doi.org/10.1063/5.0215608.

[16] U. Hampel, L. Babout, R. Banasiak, E. Schleicher, M. Soleimani, T. Wondrak, M. Vauhkonen, T. Lähivaara, C. Tan, B. Hoyle, et al., A review on fast tomographic imaging techniques and their potential application in industrial process control, Sensors 22 (6) (2022) 2309, http://dx.doi.org/10.3390/s22062309.

[17] C. Spille, V.P. Tholan, B. Straiton, M. Johannsen, M. Hoffmann, Q. Marashdeh, M. Schlüter, Electrical capacitance volume tomography (ECVT) for characterization of additively manufactured lattice structures (AMLS) in gas-liquid systems, Fluids 6 (9) (2021) 321, http://dx.doi.org/10.3390/fluids6090321.

[18] M. Wagner, C. Möller, H. Hessenkemper, M. Bieberle, U. Hampel, M. Schlüter, Hydrodynamics in cellular grid packed bubble columns disclosed with ultrafast X-ray tomography, in: Proceedings of the 8th World Congress on Industrial Process Tomography, Foz Do Iguaçu, Brazil, 2016, pp. 26–29.

[19] M. Schubert, A. Bieberle, F. Barthel, S. Boden, U. Hampel, Advanced tomographic techniques for flow imaging in columns with flow distribution packings, Chem. Ing. Tech. 83 (7) (2011) 979–991, http://dx.doi.org/10.1002/cite.201100022.

[20] L.F. Gladden, A.J. Sederman, Recent advances in flow MRI, J. Magn. Reson. 229 (2013) 2–11, http://dx.doi.org/10.1016/j.jmr.2012.11.022.

[21] L.F. Gladden, A.J. Sederman, Magnetic resonance imaging and velocity mapping in chemical engineering applications, Annu. Rev. Chem. Biomol. Eng. 8 (1) (2017) 227–247, http://dx.doi.org/10.1146/annurev-chembioeng-061114-123222.

[22] E.M. Haacke, Magnetic resonance imaging: physical principles and sequence design, 1999.

[23] M.H. Sankey, D.J. Holland, A.J. Sederman, L.F. Gladden, Magnetic resonance velocity imaging of liquid and gas two-phase flow in packed beds, J. Magn. Reson. 196 (2) (2009) 142–148, http://dx.doi.org/10.1016/j.jmr.2008.10.021.

[24] M. Sadeghi, M. Mirdrikvand, G.R. Pesch, W. Dreher, J. Thöming, Full-field analysis of gas flow within open-cell foams: comparison of micro-computed tomography-based CFD simulations with experimental magnetic resonance flow mapping data, Exp. Fluids 61 (5) (2020) 124, http://dx.doi.org/10.1007/s00348-020-02960-4.

[25] A.J. Sederman, M.L. Johns, A.S. Bramley, P. Alexander, L.F. Gladden, Magnetic resonance imaging of liquid flow and pore structure within packed beds, Chem. Eng. Sci. 52 (14) (1997) 2239–2250, http://dx.doi.org/10.1016/S0009-2509(97)00057-2.

[26] L. Huang, G. Mikolajczyk, E. Küstermann, M. Wilhelm, S. Odenbach, W. Dreher, Adapted MR velocimetry of slow liquid flow in porous media, J. Magn. Reson. 276 (2017) 103–112, http://dx.doi.org/10.1016/j.jmr.2017.01.017.

[27] D. Clarke, F. Dolamore, C.J. Fee, P. Galvosas, D.J. Holland, Investigation of flow through triply periodic minimal surface-structured porous media using MRI and CFD, Chem. Eng. Sci. 231 (2021) 116264, http://dx.doi.org/10.1016/j.ces.2020.116264.

[28] D. Clarke, P. Galvosas, D.J. Holland, Characterization of unsteady flow in a 3D-printed Schwarz Diamond monolith using magnetic resonance velocimetry, AIChE J. 69 (8) (2023) e18097, http://dx.doi.org/10.1002/aic.18097.

[29] D.A. Clarke, M.J. Coe, P. Galvosas, D.J. Holland, Investigation of turbulent flow in a Schwarz Diamond monolith using MRI and CFD, Chem. Eng. J. (2025) 168921, http://dx.doi.org/10.1016/j.cej.2025.168921.

[30] B. Dietrich, W. Schabel, M. Kind, H. Martin, Pressure drop measurements of ceramic sponges—Determining the hydraulic diameter, Chem. Eng. Sci. 64 (16) (2009) 3633–3640, http://dx.doi.org/10.1016/j.ces.2009.05.005.

[31] M. Rezapourian, R. Kumar, I. Hussainova, Effect of unit cell rotation on mechanical performance of selective laser melted Gyroid structures for bone tissue engineering, Prog. Eng. Sci. 1 (2–3) (2024) 100011, http://dx.doi.org/10.1016/j.pes.2024.100011.

[32] T. Zhang, F. Liu, K. Zhang, M. Zhao, H. Zhou, D.Z. Zhang, Numerical study on the anisotropy in thermo-fluid behavior of triply periodic minimal surfaces (TPMS), Int. J. Heat Mass Transfer 215 (2023) 124541, http://dx.doi.org/10.1016/j.ijheatmasstransfer.2023.124541.

[33] P. Kumar, F. Topin, Investigation of fluid flow properties in open cell foams: Darcy and weak inertia regimes, Chem. Eng. Sci. 116 (2014) 793–805, http://dx.doi.org/10.1016/j.ces.2014.06.009.

[34] R.K. Singh, Y. Fu, C. Zeng, D.T. Nguyen, P. Roy, J. Bao, Z. Xu, G. Panagakos, Hydrodynamics of countercurrent flow in an additive-manufactured column with triply periodic minimal surfaces for carbon dioxide capture, Chem. Eng. J. 450 (2022) 138124, http://dx.doi.org/10.1016/j.cej.2022.138124.

[35] K. Vhora, D. Thévenin, G. Janiga, K. Sundmacher, CFD analysis of the flow in Schwarz-D TPMS structures for engineering applications, Chem. Ing. Tech. 96 (12) (2024) 1683–1696, http://dx.doi.org/10.1002/cite.202400093.

[36] F. Klemens, S. Schuhmann, G. Guthausen, G. Thäter, M.J. Krause, CFD-MRI: A coupled measurement and simulation approach for accurate fluid flow characterisation and domain identification, Comput. & Fluids 166 (2018) 218–224, http://dx.doi.org/10.1016/j.compfluid.2018.02.022.

[37] D.R. Rutkowski, S.B. Reeder, L.A. Fernandez, A. Roldán-Alzate, Surgical planning for living donor liver transplant using 4D flow MRI, computational fluid dynamics and in vitro experiments, Comput. Methods Biomech. Biomed. Eng.: Imaging & Vis. 6 (5) (2018) 545–555, http://dx.doi.org/10.1080/21681163.2017.1278619.

[38] C. Wüstenhagen, K. John, S. Langner, M. Brede, S. Grundmann, M. Bruschewski, CFD validation using in-vitro MRI velocity data–Methods for data matching and CFD error quantification, Comput. Biol. Med. 131 (2021) 104230, http://dx.doi.org/10.1016/j.compbiomed.2021.104230.

[39] J.W. Fisher, S.W. Miller, J. Bartolai, T.W. Simpson, M.A. Yukish, Catalog of triply periodic minimal surfaces, equation-based lattice structures, and their homogenized property data, Data Brief 49 (2023) 109311, http://dx.doi.org/10.1016/j.dib.2023.109311.

[40] H.-Y. Lei, J.-R. Li, Q.-H. Wang, Z.-J. Xu, W. Zhou, C.-L. Yu, T.-Q. Zheng, Feasibility of preparing additive manufactured porous stainless steel felts with mathematical micro pore structure as novel catalyst support for hydrogen production via methanol steam reforming, Int. J. Hydrog. Energy 44 (45) (2019) 24782–24791, http://dx.doi.org/10.1016/j.ijhydene.2019.07.187.

[41] K. Yeranee, Y. Rao, A review of recent investigations on flow and heat transfer enhancement in cooling channels embedded with triply periodic minimal surfaces (TPMS), Energies 15 (23) (2022) 8994, http://dx.doi.org/10.3390/en15238994.

[42] J. Iyer, T. Moore, D. Nguyen, P. Roy, J. Stolaroff, Heat transfer and pressure drop characteristics of heat exchangers based on triply periodic minimal and periodic nodal surfaces, Appl. Therm. Eng. 209 (2022) 118192, http://dx.doi.org/10.1016/j.applthermaleng.2022.118192.

[43] D. Padrão, D. Hancock, J. Paterson, F. Schoofs, C. Tuck, I. Maskery, New structure-performance relationships for surface-based lattice heat sinks, Appl. Therm. Eng. 236 (2024) 121572, http://dx.doi.org/10.1016/j.applthermaleng.2023.121572.

[44] DIN Deutsches Institut für Normung e.V., Stainless steel components for aseptic applications in the chemical and pharmaceutical industry – Tubes, 2016, DIN 11866:2016-11.

[45] DIN Deutsches Institut für Normung e.V., Stainless steel components for hygienic and aseptic applications in the food, the chemical and the pharmaceutical industries – Clamp connections with molded seals, 2025, DIN 32676:2025-09.

[46] DIN Deutsches Institut für Normung e.V., Additive Fertigung Grundlagen – Terminologie (ISO/ASTM 52900:2021), 2022, Deutsche Fassung EN ISO/ASTM 52900:2021. 52900:2022-03.

[47] Endress+Hauser, Proline Promass 80, 2025, https://bdih-download.endress.com/files/DLA/50721CA194500164E10000000A35E042/BA00057DDE_1312.pdf. (Accessed 22 December 2025).

[48] M. Hawken, S. Reid, D. Clarke, M. Watson, C. Fee, D. Holland, Characterization of pressure drop through Schwarz-Diamond triply periodic minimal surface porous media, Chem. Eng. Sci. 280 (2023) 119039, http://dx.doi.org/10.1016/j.ces.2023.119039.

[49] P. Novotny, O. Sohnel, Densities of binary aqueous solutions of 306 inorganic substances, J. Chem. Eng. Data 33 (1) (1988) 49–55, http://dx.doi.org/10.1021/je00051a018.

[50] P. Stephan, S. Kabelac, M. Kind, D. Mewes, K. Schaber, T. Wetzel, VDI-Wärmeatlas: Fachlicher Träger VDI-Gesellschaft Verfahrenstechnik und Chemieingenieurwesen, Springer-Verlag, 2013, http://dx.doi.org/10.1007/978-3-642-19981-3.

[51] M. Motin, Temperature and concentration dependence of apparent molar volumes and viscosities of NaCl, NH4Cl, CuCl2, CuSO4, and MgSO4 in pure water and water+ urea mixtures, J. Chem. Eng. Data 49 (1) (2004) 94–98, http://dx.doi.org/10.1021/je0340957.

[52] A. Dybbs, R. Edwards, A new look at porous media fluid mechanics—Darcy to turbulent, Fundam. Transp. Phenom. Porous Media (1984) 199–256, http://dx.doi.org/10.1007/978-94-009-6175-3_4.

[53] B.D. Wood, X. He, S.V. Apte, Modeling turbulent flows in porous media, Annu. Rev. Fluid Mech. 52 (1) (2020) 171–203, http://dx.doi.org/10.1146/annurev-fluid-010719-060317.
[54] E.L. Que, E. Gianolio, S.L. Baker, A.P. Wong, S. Aime, C.J. Chang, Copper-responsive magnetic resonance imaging contrast agents, J. Am. Chem. Soc. 131 (24) (2009) 8527–8536, http://dx.doi.org/10.1021/ja900884j.
[55] P.T. Callaghan, Translational Dynamics and Magnetic Resonance: Principles of Pulsed Gradient Spin Echo NMR, Oxford University Press, 2011.
[56] C. D'Agostino, P. Bräuer, P. Charoen-Rajapark, M.D. Crouch, L.F. Gladden, Effect of paramagnetic species on T 1, T 2 and T 1/T 2 NMR relaxation times of liquids in porous CuSO 4/Al 2 O 3, RSC Adv. 7 (57) (2017) 36163–36167, http://dx.doi.org/10.1039/C7RA07165E.
[57] E.K. Fram, R.J. Herfkens, G.A. Johnson, G.H. Glover, J.P. Karis, A. Shimakawa, T.G. Perkins, N.J. Pelc, Rapid calculation of T1 using variable flip angle gradient refocused imaging, Magn. Reson. Imaging 5 (3) (1987) 201–208, http://dx.doi.org/10.1016/0730-725x(87)90021-x.
[58] P.T. Callaghan, Principles of Nuclear Magnetic Resonance Microscopy, Clarendon Press, 1993.
[59] J.-P. Korb, R.G. Bryant, Magnetic field dependence of proton spin-lattice relaxation times, Magn. Reson. Med.: Off. J. Int. Soc. Magn. Reson. Med. 48 (1) (2002) 21–26, http://dx.doi.org/10.1002/mrm.10185.
[60] W.D. Rooney, G. Johnson, X. Li, E.R. Cohen, S.-G. Kim, K. Ugurbil, C.S. Springer, Jr., Magnetic field and tissue dependencies of human brain longitudinal 1h2o relaxation in vivo, Magn. Reson. Med.: Off. J. Int. Soc. Magn. Reson. Med. 57 (2) (2007) 308–318, http://dx.doi.org/10.1002/mrm.21122.
[61] M. O'Donnell, NMR blood flow imaging using multiecho, phase contrast sequences, Med. Phys. 12 (1) (1985) 59–64, http://dx.doi.org/10.1118/1.595736.
[62] J. Lee, S. Ko, J.-H. Cho, S. Song, Validation of magnetic resonance velocimetry for mean velocity measurements of turbulent flows in a circular pipe, J. Mech. Sci. Technol. 31 (3) (2017) 1275–1282, http://dx.doi.org/10.1007/s12206-017-0226-x.
[63] J.R. Kroeger, F.C. Pavesio, R. Mörsdorf, K. Weiss, A.C. Bunck, B. Baeßler, D. Maintz, D. Giese, Velocity quantification in 44 healthy volunteers using accelerated multi-VENC 4D flow CMR, Eur. J. Radiol. 137 (2021) 109570, http://dx.doi.org/10.1016/j.ejrad.2021.109570.
[64] A.T. Lee, G. Bruce Pike, N.J. Pelc, Three-point phase-contrast velocity measurements with increased velocity-to-noise ratio, Magn. Reson. Med. 33 (1) (1995) 122–126, http://dx.doi.org/10.1002/mrm.1910330119.
[65] P. Irarrazaval, A.D. Firoozabadi, S. Uribe, C. Tejos, C. Sing-Long, Noise estimation for the velocity in MRI phase-contrast, Magn. Reson. Imaging 63 (2019) 250–257, http://dx.doi.org/10.1016/j.mri.2019.08.028.
[66] M. Sangal, M. Anikeeva, S.C. Priese, H. Mattern, J.-B. Hövener, O. Speck, MR based magnetic susceptibility measurements of 3D printing materials at 3 Tesla, J. Magn. Reson. Open 16 (2023) 100138, http://dx.doi.org/10.1016/j.jmro.2023.100138.
[67] J. Spurk, N. Aksel, Fluid Mechanics, Springer Cham, 2020, http://dx.doi.org/10.1007/978-3-030-30259-7.
[68] M. Matyka, Z. Koza, How to calculate tortuosity easily? in: AIP Conference Proceedings, vol. 1453, American Institute of Physics, 2012, pp. 17–22, http://dx.doi.org/10.1063/1.4711147.
[69] T. Merbach, M. Adrian, C. Wigger, S. Iraqi Houssaini, B. Bayer, A. Tsanda, S. Acikgöz, Data supplement for publication: Comprehensive study of 3D flow fields in additively manufactured structures for SMART reactors using large-scale vertical magnetic resonance imaging and computational fluid dynamics, 2026, http://dx.doi.org/10.15480/882.16072.
[70] P.J. Roache, Quantification of uncertainty in computational fluid dynamics, Annu. Rev. Fluid Mech. 29 (1) (1997) 123–160, http://dx.doi.org/10.1146/annurev.fluid.29.1.123.
[71] L.F. Richardson, J.A. Gaunt, VIII. The deferred approach to the limit, Philos. Trans. R. Soc. Lond. Ser. A, Contain. Pap. A Math. Phys. Character 226 (636–646) (1927) 299–361, http://dx.doi.org/10.1098/rsta.1927.0008.
[72] M. Bruschewski, D. Freudenhammer, W.B. Buchenberg, H.-P. Schiffer, S. Grundmann, Estimation of the measurement uncertainty in magnetic resonance velocimetry based on statistical models, Exp. Fluids 57 (5) (2016) 83, http://dx.doi.org/10.1007/s00348-016-2163-3.
[73] M. Bruschewski, S. Flint, S. Becker, Magnetic resonance velocimetry measurement of viscous flows through porous media: comparison with simulation and voxel size study, Physics 3 (4) (2021) 1254–1267, http://dx.doi.org/10.3390/physics3040079.
[74] K.R. O'Brien, B.R. Cowan, M. Jain, R.A. Stewart, A.J. Kerr, A.A. Young, MRI phase contrast velocity and flow errors in turbulent stenotic jets, J. Magn. Reson. Imaging: Off. J. Int. Soc. Magn. Reson. Med. 28 (1) (2008) 210–218, http://dx.doi.org/10.1002/jmri.21395.
[75] R. Fučík, R. Galabov, P. Pauš, P. Eichler, J. Klinkovskỳ, R. Straka, J. Tintěra, R. Chabiniok, Investigation of phase-contrast magnetic resonance imaging underestimation of turbulent flow through the aortic valve phantom: Experimental and computational study using lattice Boltzmann method, Magn. Reson. Mater. Phys. Biology Med. 33 (5) (2020) 649–662, http://dx.doi.org/10.1007/s10334-020-00837-5.
[76] M. Correia de Verdier, J. Berglund, J. Wikström, Effect of MRI acquisition parameters on accuracy and precision of phase-contrast measurements in a small-lumen vessel phantom, Eur. Radiol. Exp. 8 (1) (2024) 45, http://dx.doi.org/10.1186/s41747-024-00435-3.
[77] J. Zhou, M. Ding, Z. Meng, Y. Zhang, Z. Sun, Reducing the flow distribution in central-type compact parallel flow heat exchangers having optimized tube structure, Front. Energy Res. 6 (2018) 35, http://dx.doi.org/10.3389/fenrg.2018.00035.
[78] K. John, S. Jahangir, U. Gawandalkar, W. Hogendoorn, C. Poelma, S. Grundmann, M. Bruschewski, Magnetic resonance velocimetry in high-speed turbulent flows: sources of measurement errors and a new approach for higher accuracy, Exp. Fluids 61 (2) (2020) 27, http://dx.doi.org/10.1007/s00348-019-2849-4.
[79] S. Romig, K. John, S. Schmidt, S. Schmitter, S. Grundmann, M. Bruschewski, Improving MRI turbulence quantification by addressing the measurement errors caused by the derivatives of the turbulent velocity field–Sequence development and in-vitro validation, Magn. Reson. Imaging 117 (2025) 110333, http://dx.doi.org/10.1016/j.mri.2025.110333.
[80] R. Evans, C.R. Timmel, P. Hore, M.M. Britton, Magnetic resonance imaging of the manipulation of a chemical wave using an inhomogeneous magnetic field, J. Am. Chem. Soc. 128 (22) (2006) 7309–7314, http://dx.doi.org/10.1021/ja0608287.
[81] M.R. Serial, S. Benders, P. Rotzetter, D.L. Brummerloh, J.P. Metzger, S.P. Gross, J. Nussbaum, C.R. Müller, K.P. Pruessmann, A. Penn, Temperature distribution in a gas-solid fixed bed probed by rapid magnetic resonance imaging, Chem. Eng. Sci. 269 (2023) 118457, http://dx.doi.org/10.1016/j.ces.2023.118457.